Effectiveness of Mitigation Strategies for Wastewater-Injection-Induced Seismicity to Reduce Seismic Risk

by

Eric Gregory Johnson

A thesis submitted to the

Faculty of the Graduate School of the

University of Colorado in partial fulfillment

of the requirement for the degree of

Master of Science

Department of Civil, Environmental and Architectural Engineering

2020

This thesis entitled:

Effectiveness of Mitigation Strategies for Wastewater-Injection-Induced

Seismicity for Reducing Seismic Risk

written by Eric Gregory Johnson

has been approved for the Department of Civil, Environmental and

Architectural Engineering

_____

Prof. Abbie B. Liel

_____

Prof. Harihar Rajaram

_____

Dr. Nicolas Luco

Date _____

The final copy of this thesis has been examined by the signatories, and we find

that both the content and the form meet acceptable presentation standards of

scholarly work in the above-mentioned discipline.

Abstract

Johnson, Eric G. (M.S., Civil, Environmental and Architectural Engineering)

Effectiveness of Mitigation Strategies for Wastewater-Injection-Induced Seismicity for Reducing Seismic Risk

Thesis directed by Associate Professor Abbie B. Liel

Over the past decade, the central United States has experienced elevated rates of earthquake occurrence and, correspondingly, damage to the built environment. Experts agree that this increase in seismicity is caused by deep injection of wastewater from oil and gas processes. The disposal of this wastewater increases pore pressures, and can cause slip on faults in the basement, producing earthquakes that are anthropogenic in origin. In response to the increasing seismicity, a few mitigation strategies have been proposed and implemented. The most basic strategy is an overall injection volume reduction, such as the 2016 response plan implemented in Oklahoma instructing an overall reduction of 40% in injection volumes. Another commonly used method is referred to as a traffic light system; under a traffic light system, if an earthquake with a particular magnitude or causing shaking exceeding some

ground motion threshold occurs, injection operations are altered. A third strategy is increasing well spacing to limit well interactions.

This study examines these mitigation strategies and quantifies their influence on seismic risk to the built environment. To conduct this study, a hydromechanical model is used to simulate earthquake occurrence in time and space. The magnitude of the events are stochastically generated from a Gutenberg-Richter distribution. For each earthquake, we use a ground motion prediction equation for the central United States to determine spectral accelerations for sites within the study region. To evaluate seismic risk, the spectral accelerations are input to vulnerability or loss curves for wood frame buildings common in the central United States. These curves quantify earthquake-induced repair costs. By varying input parameters on injection rates and well spacing, the impact on risk of each of these systems is compared.

The results show that increasing the distance between injection wells is the most effective strategy for reducing seismicity while also causing the least interruption in injection operations. Traffic light systems and overall injection reduction also reduce seismicity, with overall reduction being more effective when comparing earthquake count to injected volume. I also find that exclusion zones are very effective at limiting risk.

Acknowledgments

I would first like to thank my advisor, Professor Abbie Liel. Every step of the project has been a great experience thanks to her support and guidance. I'm particularly thankful for her patience in the early stages of the project, before I had a background in the fields of earthquake engineering and induced seismicity.

Thank you also to the Colorado Collaboratory for Induced Seismicity. It has been fascinating being involved with this group and learning about everything that ties into induced seismicity issues.

Thank you to the Liel Research Group, past and present. Currently this group consists of Dustin, Polly, Zach, Casie, Hailey-Rae, Briar, and Janice and they have all been immensely supportive regarding research and otherwise.

I would like to acknowledge the contributions of Bridger Baird and Ryan Haagenson. I have applied Bridger's results for drift and floor accelerations for light frame wood single- and multi-family buildings for determining structural loss given ground motion. Ryan has spent a great amount of time creating, adapting, and refining the hydromechanical model I use to produce earthquake catalogs for different injection scenarios.

Thank you to my friends from my hometown, from the University of Delaware, and from the University of Colorado Boulder. I know I can rely on you all for some levity when I'm stressed with school or finding a career.

Finally, I would like to thank my father, Greg; my mother, Ellen; my sister, Kerry; her husband, David; and their daughter, Harper. Your support has been incredible.

Table of Contents

List of Tables

List of Figures

1 Introduction

The central United States, particularly Oklahoma and the surrounding region, have experienced over a decade of greatly heightened seismicity. Researchers have attributed this seismicity mostly to deep injection of wastewater from oil and gas operations. While mostly of small to moderate magnitude, some of these human-induced earthquakes have caused damage to buildings in communities in oil and gas producing areas. In particular, several earthquakes in Oklahoma, including the 2011 M_w5.7 Prague, the 2016 M_w5.8 Pawnee, and the 2016 M_w5.0 Cushing earthquakes, damaged residential structures, as well as other infrastructure (Barba-Sevilla et al., 2018; Chase et al., 2019; Keranen & Weingarten, 2018). In the Groningen Oil Fields in the Netherlands, small earthquakes, up to M_L 3.6, have damaged buildings (Keranen & Weingarten, 2018; van Thienen-Visser & Breunese, 2015).

A number of strategies have been proposed to limit or reduce the seismic hazard from injection-induced seismicity by adjusting wastewater injection operations. This study couples a hydromechanical model of earthquake generation with earthquake-engineering ground motion and loss models to compare three mitigation strategies to evaluate which are most effective at reducing risk to the surrounding community and region. The mitigation strategies considered are: increasing separation distances between injection wells, reducing the injection rate of all wells by a set percentage, and applying a magnitude-reactive "traffic light" system that also reduces injection rate.

To explore these mitigation strategies, I first use a hydromechanical model of the injection wells and surrounding area to model pore pressure diffusion in order to produce earthquake catalogs for a given injection/mitigation scenario over a two-year period. I then investigate the effects of these earthquake catalogs, using a ground motion model to estimate earthquake intensities over the region for each earthquake. I use a loss model to assess repair costs for individual buildings and groups of buildings for each injection scenario. For this study, I quantify seismic risk in terms of earthquake-induced economic losses (i.e., repair costs) to wood frame single- and multi-family housing, the most common building type in the central United States. I then compare the mitigation strategies based on how they affect risk on a local scale and on a regional scale, while ideally, not greatly impacting the injection operation. The location, wells and communities in this study are generic, but represent Northern Oklahoma or Southern Kansas in terms of both geophysical properties and building exposure and fragility. Therefore, the risk metrics and loss values are most useful in a comparative sense.

This thesis is organized as follows. Following this introduction, Chapter Two discusses the current state of research in wastewater-injection-induced earthquake hazard and risk and earthquake mitigation strategies for new or existing injection regions and the relation between this study and the state of research. Chapter Three explains the methods applied and the models created for this study. Chapter Four describes the findings. Chapter Five summarizes

the results of this study, offers suggestions for applying this research, and

discusses possible future work.

2 Literature Review

2.1 Seismicity Associated with Wastewater Injection

Oklahoma and other parts of the central United States have experienced a significant increase in seismicity, relative to background levels, for over a decade. As summarized in Jones (2020), until 2008, the state would see $2 - 3$ magnitude 3.0 or greater earthquakes per year. The rate of seismicity started increasing in 2009 with 20 earthquakes of magnitude 3.0 or above. The peak year of this earthquake swarm was 2015, with 903 earthquakes above magnitude 3.0, and 27 greater than magnitude 4.0. More recently, the rate has been decreasing due to mitigation efforts and a decline in oil prices and production (Roach, 2018). In 2019, Oklahoma saw 62 earthquakes of $M_w3.0$ or greater and one above $M_w4.0$. These statistics are particularly noteworthy when considering that California, a state over twice as large as Oklahoma (*State Area Measurements and Internal Point Coordinates*, 2018) and historically more seismic (Toppozada et al., 2002; Working Group on California Earthquake Probabilities, 1995), sees an average of about 258 $M_w3.0$ or greater earthquakes per year (*Lists, Maps, and Statistics*, 2016). Oklahoma experienced a four-year period from $2014 - 2017$ in which the state annually exceeded 300 $M_w3.0$ or greater earthquakes.

This increase in seismicity is anthropogenic. Earthquakes attributed to hydraulic fracturing have been observed in the Western Canadian Sedimentary Basin (Atkinson et al., 2016; Rubinstein & Mahani, 2015) and, more recently,

in the SCOOP (**S**outh **C**entral **O**klahoma **O**il **P**rovince) and STACK (**S**ooner **T**rend - oil field, **A**nadarko - basin, **C**anadian, and **K**ingfisher - counties) plays in Oklahoma (Skoumal et al., 2018). Earthquakes across the world have also been attributed to enhanced oil recovery (Frohlich et al., 2016; Rubinstein & Mahani, 2015), enhanced geothermal systems (Keranen & Weingarten, 2018; Lee et al., 2019; Majer et al., 2012), carbon capture and storage (Keranen & Weingarten, 2018; McGarr et al., 2015), and gas extraction (van Thienen-Visser & Breunese, 2015; Vlek, 2019).

However, the primary source of induced earthquakes in the central United States is wastewater injection (Atkinson et al., 2016; Rubinstein & Mahani, 2015). Wastewater injection as a cause for earthquakes was first observed at the Rocky Mountain Arsenal in Denver, Colorado (Healy et al., 1968). The contents of wastewater produced by oil drilling vary by region. In Ohio and Arkansas, it is primarily made up of spent hydraulic fracturing fluid, but in Oklahoma and other regions with less hydraulic fracturing, the fluid consists of mostly produced water from oil extraction (Rubinstein & Mahani, 2015). Wastewater injection has become significantly more extensive in the past 15 years or so. In fact, from 2004 to 2008, wastewater injection in Oklahoma nearly doubled (Keranen et al., 2014). The monthly injected volume leveled out from 2008 until 2012, before sharply increasing to a peak in 2015; injection has been declining since then (Langenbruch et al., 2018). By 2018, injection volumes had decreased to less than 50% of 2015 volumes (Langenbruch et al., 2018).

Fluid injection increases pore water pressures and reduces normal stress, moving critically stressed faults towards Coulomb failure criteria (Raleigh et al., 1976). These events can be triggered by as low as a 0.01 MPa change in stress (Goebel et al., 2017; McGarr et al., 2002; Shapiro, 2015). Earthquakes can occur immediately if injection is directly into the crystalline basement or in a region where fractures link the injection to faults (Keranen & Weingarten, 2018; McGarr et al., 2015). More typically, however, there is a delay between injection and seismicity as pore pressure diffuses to faults over the time scale of weeks to months, or even years; a termination in injection will not lead to an immediate cessation in seismicity as the increased pressure takes time to dissipate (Keranen & Weingarten, 2018).

2.2 Influence of Injection-Induced Earthquakes on Seismic Hazard

Seismic hazard defines the probability of reaching or exceeding a ground motion intensity of interest at a particular location (Cornell, 1968). Seismic hazard can be associated with either natural or operational hazard. Natural seismic hazard is a factor of geology, geomechanical state, and earthquake history (Walters et al., 2015). Operational seismic hazard depends on injection operations, formation characteristics (in particular, whether the injection formation is connected to the basement or if it is underpressured), and the monitoring level of the region (Walters et al., 2015). Higher rate injection wells, meaning greater volume of injected fluid per day, have been shown to increase seismic hazard (Keranen et al., 2014).

The United States Geological Survey (USGS) produces seismic hazard models for the United States. One model is the National Seismic Hazard Map (NSHM), which was most recently updated in 2018 (Petersen et al., 2019). The USGS excludes suspected induced earthquakes on the NSHM, because induced earthquakes are considered to be transient and not appropriate for a long-term model (Petersen et al., 2014, 2019). Instead, the USGS has produced three one-year hazard maps for induced seismicity (Petersen et al., 2016, 2017, 2018). These maps have areas with up to three times greater hazard than the prior (2014) NSHM (Petersen et al., 2016). The first map, 2016, gave a 5% – 12% probability of a damaging (MMI VI+) earthquake per year in North-Central Oklahoma and Southern Kansas (Petersen et al., 2016). The one-year hazard is forecast considering primarily the previous year's catalog, but also a catalog of the past two years and a long-term catalog, and a Gutenberg-Richter distribution (Petersen et al., 2018; White et al., 2018). It considers injection only indirectly through the inclusion of data from previous years' earthquakes that have been caused by injection.

Several other studies have also developed seismicity forecasts for the Central United States (CUS). Langenbruch et al. (2018) developed a regional hybrid physical-statistical model and assessed how seismic hazard varied in space and time. They model 809 injection wells over a 145,000 km² region of Oklahoma and Kansas. They use a "seismogenic index" value as a proxy for existing fault locations and stress state. Forecasting from 2017, due to the reduced injection rate as of September 2018, they see an annual decrease in

number of earthquakes and in the probability of an event of magnitude 5.0 or greater at least through 2020 (Langenbruch et al., 2018).

Dempsey and Riffault (2019) considered a different approach from the seismogenic index, coupling pressure diffusion models to steady-state pressurization and rate-state triggering models. They chose to simplify their model of Western Oklahoma by not considering well or fault locations or material heterogeneity, but a homogenous region with evenly distributed injection in a circular region. Instead of forecasting an ongoing decrease in seismicity as in Langenbruch et al. (2018), Dempsey and Riffault (2019) see an eventual increase some time into their model. The increasing seismicity rate occurs when the pressurization rate in the basement reaches a new equilibrium. To avoid this future increase, Dempsey and Riffault (2019) recommend that injection is further cut beyond the OCC mandated 40%.

2.3 Consequences of Injection-Induced Earthquakes

While small, induced earthquakes have been observed to cause damage to structures. In 2011, a Mw5.7 earthquake near Prague, Oklahoma caused damage to homes (Keranen et al., 2013; Keranen & Weingarten, 2018). In 2016, a Mw5.8 earthquake near Pawnee, Oklahoma (the largest induced earthquake in Oklahoma), also led to damage in the region. This earthquake caused cracks and partial collapse of unreinforced masonry and brick facades as well as damage to light-frame wood buildings (Chase et al., 2019). This earthquake also affected the local groundwater systems (Keranen &

Weingarten, 2018; Yeck et al., 2017). Following this earthquake, six buildings were declared uninhabitable (Yeck et al., 2017). Later that year, a Mw5.0 earthquake in Cushing, Oklahoma led to cracks in mortar joints, brick spalling, broken utilities, damage to brick chimneys, and structural racking (Baird et al., 2020; Barba-Sevilla et al., 2018; Taylor et al., 2017).

Outside of the United States, building and infrastructure damage has been caused by gas extraction operations in the Groningen Oil Field in the Netherlands. The earthquakes around Groningen have been much smaller (the largest to date was a M_L3.6 in 2012) than the largest ones of Oklahoma. However, these small earthquakes have still damaged structures in the area (Keranen & Weingarten, 2018; van Thienen-Visser & Breunese, 2015). In this region, these lower magnitude earthquakes are capable of causing damage because of shallow event depth and soft surface soil in the region as well as limited seismic detailing in the building stock (van Thienen-Visser & Breunese, 2015; Vlek, 2019). These earthquakes have even been related to stress-related health concerns (Vlek, 2019).

Several studies have been done to analytically examine the consequences of induced earthquakes using simulation models. Harvey et al. (2017) considered fragility curves for bridges to determine that slight-to-moderate damage is possible to bridges in Oklahoma from induced ground motions.

Baird et al. (2020) used the Timber3D structural analysis platform to simulate seismic response of modern residential light-frame wood buildings in

induced earthquake scenarios. The study focused on buildings representative of modern construction in the CUS. They found that induced earthquakes of $M_w4.75$ can damage buildings over a 3 mile radius and a M_w6 can damage buildings over a 22 mile radius from the earthquake epicenter (Baird et al., 2020). These radii provide information about population exposure, which is an important factor for seismic risk (e.g., Bommer et al., 2015). However, they expect damage to be greater for older wood frame buildings and for masonry buildings.

Chase et al. (2019) examined how damage and vulnerability accumulate over a sequence of small to moderate magnitude induced earthquakes, focusing again on wood frame residential construction. They found that structures do not become more vulnerable over multiple induced events, meaning that damage in one event does not seem to impair performance in a subsequent event. However, the damage (in terms of crack size) does tend to increase with each event. Therefore, repair costs or economic losses are driven by the largest earthquake of the sequence; if the homeowner chooses to repair after each event, the total repair cost will be significantly greater (Chase et al., 2019).

Liu et al. (2019) compared collapse risk and falling risk for noncritical nonstructural components from the 2016 USGS one-year hazard model to hazards presented in the 2014 National Seismic Hazard Map. They found that collapse risk in Oklahoma City, Oklahoma and Dallas, Texas could be from 10

to over 100 times greater than from the 2014 National Seismic Hazard Model, which excludes induced seismicity (Liu et al., 2019).

2.4 Mitigation Strategies for Injection-Induced Seismicity

A number of mitigation strategies have been proposed or adopted to control the different factors that affect seismic risk associated with injection-induced seismicity, including hazard, exposure, and fragility. Here, I describe mitigation strategies for both new and existing injection operations. Sections 2.4.1 through 2.4.3 outline strategies intended for new injection regions and sections 2.4.4 through 2.4.6 outline strategies intended for existing injection regions.

2.4.1 Well Spacing Requirements

One strategy for reducing hazard is to require greater distances between injection wells. When wells are close to each other, a point between the wells will see well-to-well interactions, with both wells contributing to increases in pore pressure. Greater spacing between wells is hypothesized to limit well-to-well interactions (Brown et al., 2017).

2.4.2 Injection Depth Requirements

Wells injecting closer to the crystalline basement have greater associated hazard. When wells are directly linked to the basement faults, seismicity can be almost instant (Keranen & Weingarten, 2018; McGarr et al., 2015). It has been proposed that isolating injection further from the basement will lead to less earthquake events (Brown et al., 2017; Hincks et al., 2018). However, a case

study in Greeley, Colorado found that cementing the lowest section of the injection interval (and thereby raising injection depth further from the basement and reducing connectivity to basement) did not affect seismicity rates because of the continued injection from other more distant wells (Brown et al., 2017).

2.4.3 Well Siting Requirements

Requirements for new injection operations could significantly reduce exposure. Injection-induced seismicity typically occurs close to the injection well and attenuates rapidly (Bommer et al., 2015). Siting new wells away from population centers, critical infrastructure, or high risk facilities could greatly decrease their exposure (Brown et al., 2017; McGarr et al., 2015; Meier et al., 2015). Mutz (2019)'s review of regulations in seven states found that, of these, Ohio does not allow Class II underground injection wells within designated distances from various categories of buildings and transportation infrastructure, though the distances are short (<100 ft).

Atkinson (2017) proposed exclusion zones of a 5 kilometer radius around critical infrastructure in which hydraulic fracturing operations cannot operate and a further radius of 25 kilometers in which increased monitoring and a reactive system should be active. Baird et. al (2020) also suggest an exclusion zone would greatly decrease the hazard to critical infrastructure. Specifically, they suggest a zone of 6-10 miles for limiting major damage or 15-25 miles for lower damage thresholds. Population relocation is a possibility but could be

expensive and undesirable in many situations (Bommer et al., 2015). Siting locations are plausible for wastewater disposal but unrealistic for some other causes of induced seismicity. For instance, enhanced geothermal systems would not be able to take advantage of large exclusion zones around an operation because of inefficient energy transfer over distance and requires the operation to be near population centers (Bommer et al., 2015).

Risk matrices, as proposed by Walters et al. (2015) could be used when selecting a location for an injection operation. These matrices consider hazard, exposure, and "operational factors" to recommend favorable sites. They define their operational factors to be population density, nearby infrastructure, and local risk tolerance for a proposed site for an injection operation. They suggest that some regions are more receptive to greater risks considering benefits of the oil or gas operations (Walters et al., 2015).

2.4.4 Structural Strengthening

For areas that are already experiencing induced seismicity, Bommer et al. (2015) recommend to reduce risk by strengthening the building stock of the region with greatest hazard. Much research has been done in earthquake engineering on structural earthquake resistance, and the value of seismic detailing is well documented and codified. Bommer et al. (2015) argue that strengthening of structures is considerably less uncertain than attempting to control hazard. However, strengthening components, particularly non-structural, to avoid damage could be prohibitively expensive (Bommer et al.,

2015). While Bommer et al. (2015) acknowledge that the procedures could be disruptive, they suggest the disruptions would be better tolerated if the living or working space is improved during the renovation. Van Elk et. al (2019) suggest that selectively strengthening the buildings most likely to be damaged in conjunction with production regulations could greatly reduce risk around the Groningen Oil Fields.

2.4.5 Regional Injection Reduction

Because the overall quantity of wastewater injection is the driving factor for most of the earthquakes in the CUS, reducing injection volumes may reduce risk. Langenbruch and Zoback (2016) showed that, as injection rates in Oklahoma increased starting in 2012, the monthly number of earthquakes exceeding magnitude 3.0 followed the same trend with a degree of time lag as the region responded to the change in operations. In 2016, the Oklahoma Corporation Commission (OCC), the governing body regulating wastewater injection in Oklahoma, called for a 40% reduction in injection volume compared to 2014 levels (Skinner, 2016a, 2016b). The goal of this 40% reduction was to return the rate of injection volume per unit area to approximately 2009 levels, before the spike in seismicity in the region (Langenbruch & Zoback, 2016).

Nevertheless, the largest earthquake in Oklahoma history, the 2016 M_w5.8 Pawnee earthquake, occurred after the mandate (Yeck et al., 2017). However, the occurrence of this earthquake does not necessarily indicate that

the action was a failure. The seismic reduction was not expected to be immediate; there is a time lag as the injectate diffuses through the injection formation (Langenbruch & Zoback, 2016). In fact, there has been a coincident reduction in earthquakes, with fewer $M_w3.0$ or greater earthquakes in the state every year since the seismic peak of 2015 (Dempsey & Riffault, 2019; Jones, 2020; Langenbruch et al., 2018). As of 2018, injection volumes were down to around 45% of where they were during the seismic peak of 2015 (Langenbruch et al., 2018).

2.4.6 Traffic Light Systems

Several projects and regulatory agencies use a reactive mitigation program known as a traffic light system (TLS). This system has been used in enhanced geothermal systems, hydraulic fracturing, and wastewater disposal (Baisch et al., 2019; Bommer et al., 2015). TLSs are in use all over the world, in countries such as the Netherlands, Switzerland, Australia, and El Salvador (Baisch et al., 2019). In the United States, TLS are used in Illinois, California, Ohio, and Oklahoma, among others (Baisch et al., 2019). Traffic lights are defined by a few threshold magnitudes or ground motion intensities (Baisch et al., 2019; Bommer et al., 2015). If an injection location is at a "green light" level, with no concerning earthquake events nearby, it can operate at normal levels. After a magnitude or ground motion reaches a certain threshold, the Traffic Light guides some modifications to operations. This is a "yellow light" (or "amber light") level. If the magnitude or ground motion reaches a higher, unacceptable threshold, it is in "red light" level and the operation is suspended

(Baisch et al., 2019; Bommer et al., 2015). An operation that reaches a yellow light or red light can transition back to green light if seismicity decreases again (Walters et al., 2015).

The TLS triggering threshold must be large enough that it is not triggered unnecessarily, but low enough that it captures events that could be precursors to bigger events. To be effective, a TLS must have low triggering thresholds because it is limited by trailing effects outside of control of the operators (Baisch et al., 2019); in other words, even after the injection ceases, the pressure will continue to diffuse through the subsurface. The operators must recognize that the TLS will not become effective instantly. The $M_w5.0$ Cushing, Oklahoma earthquake occurred in an area that was utilizing a TLS (Yeck et al., 2017). This may have been allowed by a high reaction threshold. Wells were not instructed to decrease injection or stop until a series of M_w4 earthquakes had occurred (Yeck et al., 2017). Traffic lights are also limited by sparse seismic networks and a high magnitude detection threshold in the CUS (Brown et al., 2017; Walters et al., 2015). For most of the United States, the seismic network can only detect earthquakes of greater than $M_w3.0$ (McGarr et al., 2015). However, for a TLS to be effective, a minimum magnitude detection threshold of $M_w2.0$ is recommended (McGarr et al., 2015). Additionally, TLS are mostly effective for nearby earthquake swarms, near where the injection occurs. More distant swarms will not be stopped by an immediate change in pore pressure because of the time-lag in injection diffusion (Keranen & Weingarten, 2018; McGarr et al., 2015).

3 Methods

3.1 Overview

This study investigates how various mitigation strategies affect earthquake occurrence, ground shaking intensity, and economic losses to structures over a region. Fig. 3-1 demonstrates how the three primary models used work together to produce assessments of losses to buildings and regions. This chapter describes the set-up of the study region, the hydromechanical model, the methods for determination of earthquake magnitudes, the ground motion model, the loss model, and sources of uncertainty. Finally, I discuss the different mitigating injection scenarios I consider.
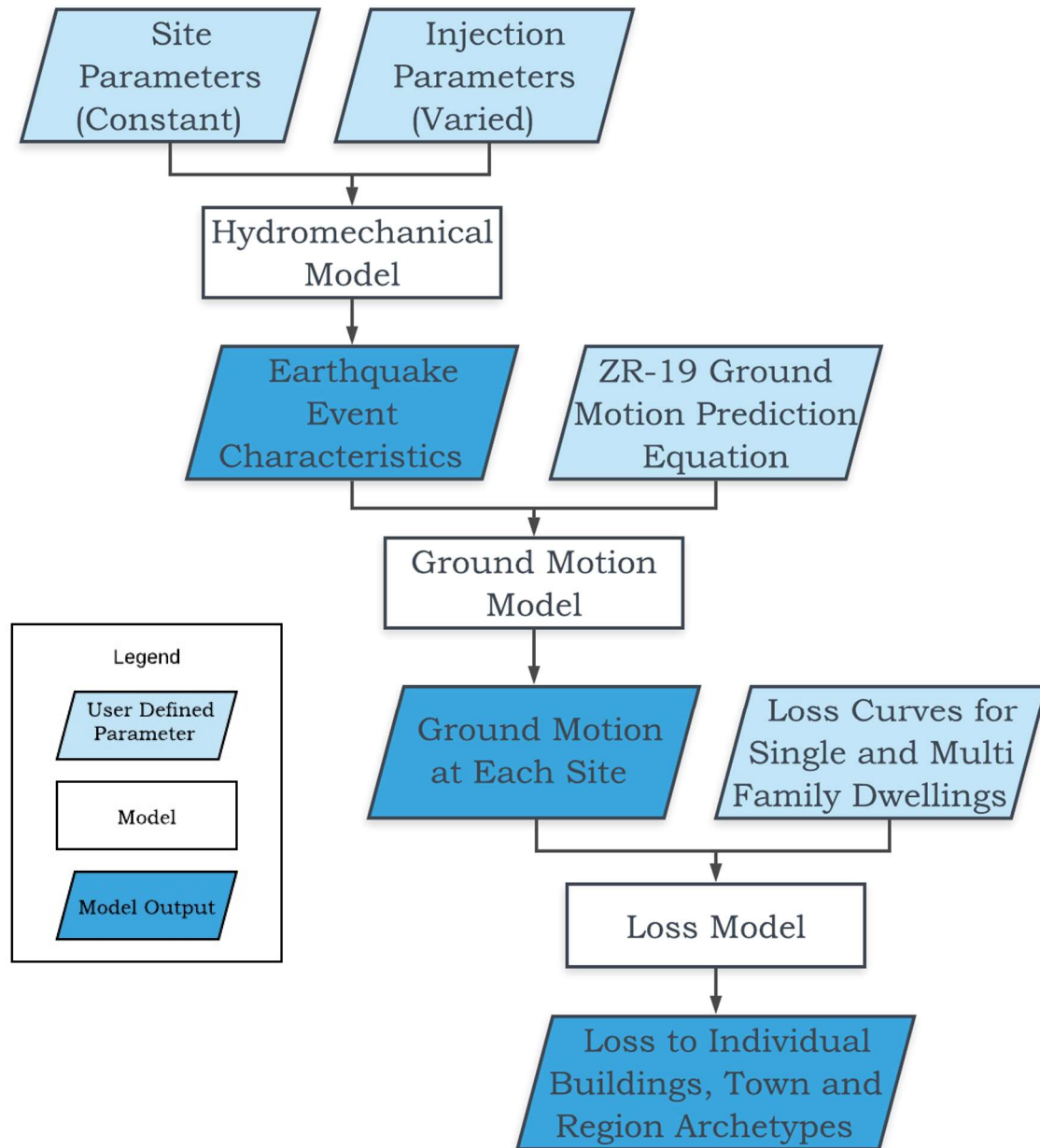
Figure 3-1 Flowchart of study framework

3.2 Study Region

The analysis region is a 120 km by 120 km square area with the injection zone occupying the middle 20 km by 20 km, as shown in Fig. 3-2.

This size was selected because the M_w5.7 Prague, OK earthquake and M_w5.8 Pawnee, OK earthquakes had an area with radii of about 50 km around the epicenter with a peak ground acceleration (PGA) of 0.05 g or greater (Gupta & Baker, 2019). Thus, my analysis region has at least 50 km of distance from every possible earthquake. For the hydromechanical and ground motion models, key geophysical properties are assumed constant through the entire analysis region. Table 3-1 outlines these properties, which are justified in more detail below.

Table 3-1 Key geophysical properties

Property	Value
V_{S30}	$450\ m/s$
Injection Layer Compressibility	$3.0 \times 10^{-10}\ Pa^{-1}$
Injection Layer Porosity	0.2
Injection Layer Permeability	$2.0 \times 10^{-14}\ m^2$
Basement Compressibility	$1.0 \times 10^{-10}\ Pa^{-1}$
Basement Porosity	0.05
Basement Permeability	$4.0 \times 10^{-14}\ m^2$

The injection zone considered is a 20 km by 20 km square region; this is also the extent of the hydromechanical model, so all earthquakes are assumed to occur within this zone, which is reasonable within the two year time period of interest. These dimensions were selected to be large enough to examine

multiple injection wells at various spacings and allow for area for pressures to diffuse outward. Within this injection zone, I have placed 16 injection wells; this number is realistic for an injection zone of this size when comparing to Oklahoma (Downey, 2017). Of these wells, eight are designated as low-rate (0.5 m³/hr) injection, four are designated as medium-rate (3 m³/hr) injection, and four are designated as high-rate (55 m³/hr) injection. These values are similar to well injection rates in 2014, the reference year for the OCC reduction mandate (Downey, 2017). Due to a limitation of the hydromechanical model, discussed later, all injection is assumed to occur at the same depth.
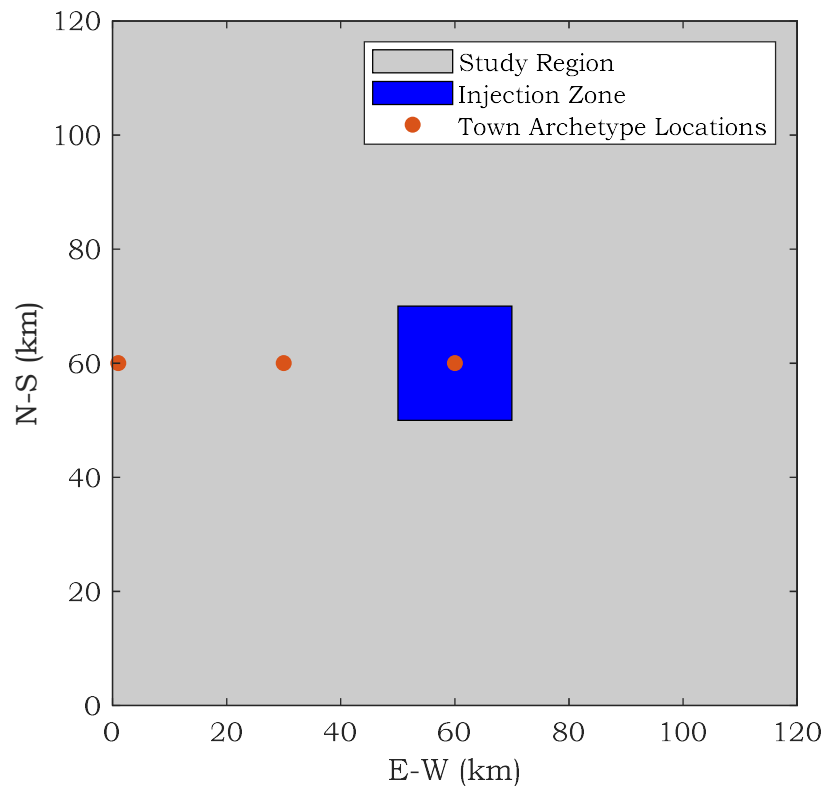
Figure 3-2 120 km x 120 km study region, with 20 km x 20 km injection zone

3.3 Hydromechanical Model

I use a hydromechanical model developed by Ryan Haagenson, following the approach used by Dempsey and Riffault (2019), to simulate mitigation injection scenarios. The Dempsey and Riffault (2019) model uses a two-dimensional (in plan) injection layer, coupled with one-dimensional vertical basement columns. Of course, fluid flow is a most often three-dimensional problem; however, such problems are computationally cumbersome. Therefore, to simplify the numerical approach while still capturing much of the relevant physics (i.e. the three-dimensional behavior), we consider a two-dimensional injection layer to represent the horizontal diffusion of pore pressure and one-dimensional vertical basement columns to represent the vertical diffusion of pore pressure, as in Dempsey and Riffault (2019). The hydromechanical model I use has hydrologic components of injectate diffusing through a porous medium and mechanical components of weak point failure defined by Mohr-Coulomb stress criterion and a lithostatic background stress state. This approach is different from the physical-statistical model used by Langenbruch et al. (2018), which modifies the Gutenberg-Richter law to consider pressure rate and seismogenic index to determine seismicity, or the model used by Dempsey and Riffault (2019) considers rate-state earthquake triggering and does not model individual wells.

The model takes inputs of hydraulic parameters of the study region, randomly generated weak points, injection locations and rates, and, when considering traffic light systems, prescribed magnitude thresholds and

reactions. The model outputs synthetic seismicity data points in time and space. Fig. 3-3 describes this process.
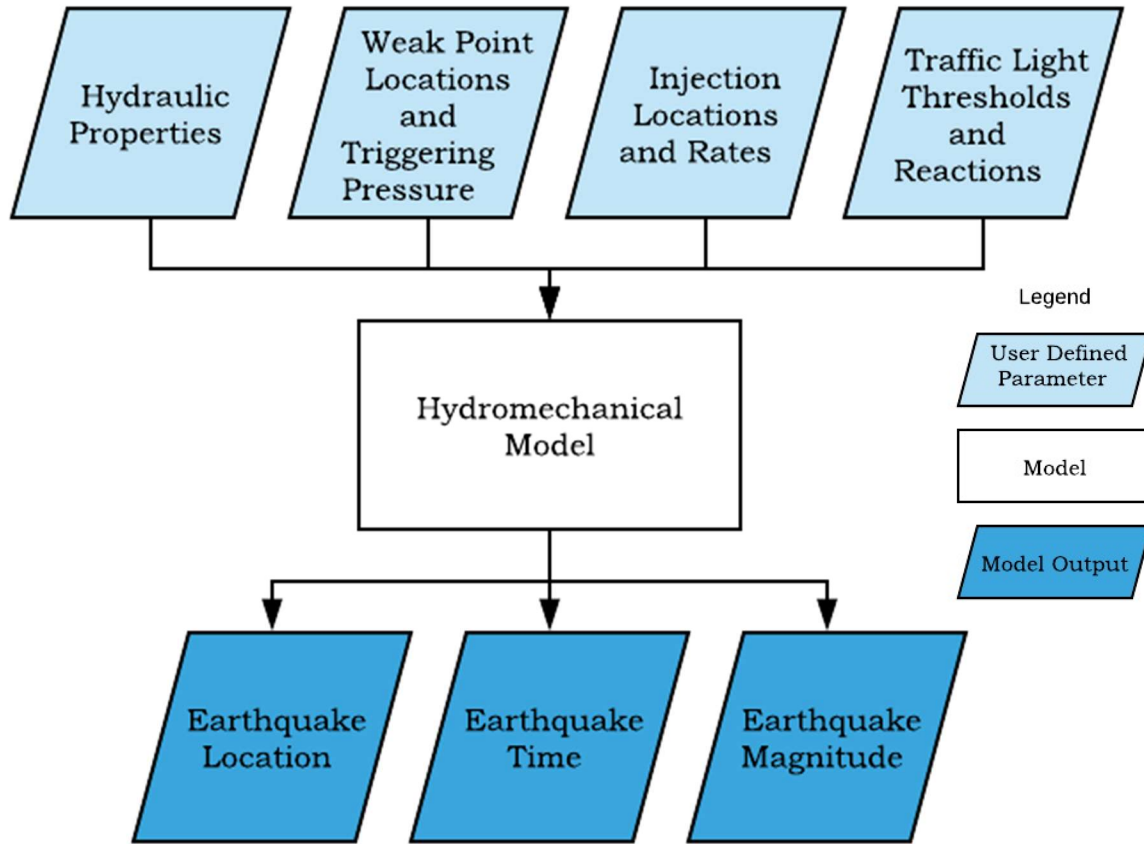
Figure 3-3 Flowchart of hydromechanical model

3.3.1 Hydrological Components of the Hydromechanical Model

The model employs a first-order Galerkin, or continuous linear, function space for the pressure solution to simulate fluid flow in the injection and basement strata. Haagenson developed this model using an open source finite element method software, FEniCS (Alnæs et al., 2015; Logg et al., 2012).

Haagenson validated this model by comparing results to the analytical

solutions for the one-dimensional problem (plane source of fluid) and Theis

problem (two-dimensional, or line source of fluid) (Carslaw & Jaeger, 1959),

showing good agreement with both solutions.

While the model presented here has some connections to the one

presented by Haagenson (2018), we have streamlined this earlier model in a

few ways for this study. In the original model, pressure diffusion is considered

to act nonlinearly, with pressure dependent fluid and hydraulic parameters.

Here, pressure diffusion is considered to act linearly, removing some

unnecessary complications, with porosity, permeability, fluid density, and all

other model parameters assumed to be constant. Our model and other similar

models (e.g. Dempsey & Riffault, 2019; Langenbruch et al., 2018) require the

assumption of constant model properties within each layer. Additionally, the

original model considers a discrete fracture network, while the updated model

removes this and considers the injection layer and basement columns to be

homogenous. We decided the discrete fracture network was excessively

complicated and did not add any value to the model outputs for the scope of

this project. Adding a fracture network would add unnecessary uncertainty in

terms of fracture parameters and geometry, and the simpler model captures

the overall effects well. To model vertical diffusion into the basement for this

study, Haagenson couples the injection layer model to many vertical one-

dimensional diffusion models, as in Dempsey and Riffault (2019). This assumes

that horizontal diffusion in the basement is negligible and that basement pressures only diffuse vertically.

The modeled region is made up of two strata: an injection layer and the crystalline basement. The injection layer is modeled as a two-dimensional 20 km by 20 km square surrounded by 7.5 km buffers on all sides for a total domain of 35 km by 35 km. The buffer distance ensures that the injection region does not see boundary effects from the applied hydrostatic boundary conditions. This model space is discretized into a structured mesh grid with vertices spaced at 50 meters. The model assumes the injection layer has a uniform thickness of 500 meters.

The basement is modeled as 400 vertical columns, each 1 km by 1 km in plan. The number of basement models was selected according to the available computational resources. The columns begin at the interface of the injection layer and extend 10 km downward to avoid boundary effects. The upper boundary condition of each basement column model is set to the pressure at the center of the 1 km by 1 km region of the injection layer the column represents. The boundary condition at the bottom is a no-flow condition. The basement columns are one-way coupled to the injection layer; flow into the basement is based on the pressures above, but the injection layer behaves as if no fluid is lost to the basement columns; hence, the model is one-way coupled. This one-way coupling is reasonable because the basement permeability is much lower than the injection layer.

To set up the model for use in simulating a generic site, the site parameters are selected to emulate the central United States. Following Birdsell et al. (2018), the basement permeability is selected to be 4.0×10^{-15} m^2. This value, while slightly higher than some other studies (Catalli et al., 2016; Dempsey & Riffault, 2019; Langenbruch et al., 2018), falls within the range for permeability considered in Brown et al. (2017). Moreover, recent research by Birdsell et al. (2018) indicates that the effective permeability of the highly fractured basement may need to be set higher than previously thought in the context of induced seismicity problems, as the fracture network dominates the hydraulic behavior. While the model results are certainly highly sensitive to the basement permeability, the goal of this project is to replicate a hypothetical subsurface and the basement permeability selected is reasonable.

3.3.2 Mechanical Components of the Hydromechanical Model

Weak point locations are randomly generated with a uniform distribution in plan and a lognormal distribution representing the Oklahoma, Southern Kansas, and Northern Texas earthquake catalog in depth (U.S. Geological Survey, n.d.). All events are assumed to occur in basement faults, so the weak point distribution for depth begins at the interface of the basement. The depth to basement was selected to be 3 km from the surface (Crain & Chang, 2018). Each weak point is randomly assigned a fracture orientation and coefficient of friction. The vertical pressure profile is assumed to be hydrostatic and the vertical stress profile is assumed to be lithostatic, with a coefficient of lateral earth pressure of 0.6; both include the effects of compressibility to account for

the change in fluid and rock density at depth. Haagenson calculates the

triggering pressure of each weak point following Mohr-Coulomb failure

criterion, assuming the fractures are essentially cohesionless. We have selected

the minimum triggering pressure to be 0.01 MPa, as this is the minimum

change in pressure that has been noted to cause induced seismicity (Gischig &

Wiemer, 2013; Goebel et al., 2017; McGarr et al., 2002; Shapiro, 2015), and we

discard weak points with triggering pressures above 0.1 MPa as they are

unlikely to trigger during the simulation. Fig. 3-4 shows how the model

progresses through time for evaluating weak point failure, including the one-

way coupling between the injection layer and basement columns.
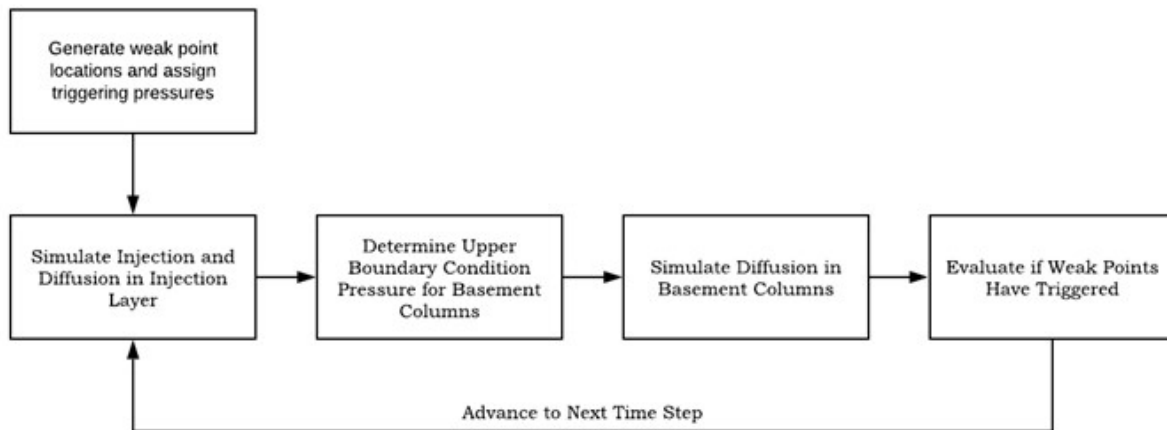
Figure 3-4 Flowchart of pressure diffusion and weak point evaluation

The hydromechanical model outputs a catalog of earthquakes for a given

injection scenario. As weak points reach their assigned triggering pressure

perturbation, the time step since the start of injection and location of the weak

point are added to the earthquake catalog. Earthquake magnitudes are assigned following a Gutenberg-Richter distribution, as described in section 3.4.

The number of weak points, a heuristic value, is the parameter that is used to calibrate the model. A greater number of weak points leads to more earthquake events being generated. My target is approximately 300 $M_w2.0+$ events over a two year span to simulate a CUS region of a similar size experiencing a large degree of seismicity, as seen in parts of Oklahoma (U.S. Geological Survey, n.d.). We adjusted the number of weak points generated until we approached this number of earthquakes.

Fig. 3-5 compares the generated earthquake depths with a catalog of 2018 Oklahoma earthquake depths (U.S. Geological Survey, n.d.). Although the weak point depth distribution was based on these empirical depths, the standard deviation of depths in the historical catalog is greater than the model and the means are different because the historical catalog considers events over a much larger area, with different geological strata depths and properties. Our modeled events are for a much smaller region, with homogenous strata depths and properties. Moreover, the historical catalogs represent seismicity over a longer time frame than was considered during our model simulations. With longer simulation times, it is likely we would see the simulated catalog become more similar to the historical (or target) catalogs because more time would be allowed for greater downward diffusion. This depth distribution may

be refined in future work by adjusting the initial stress state to better match the USGS catalog.
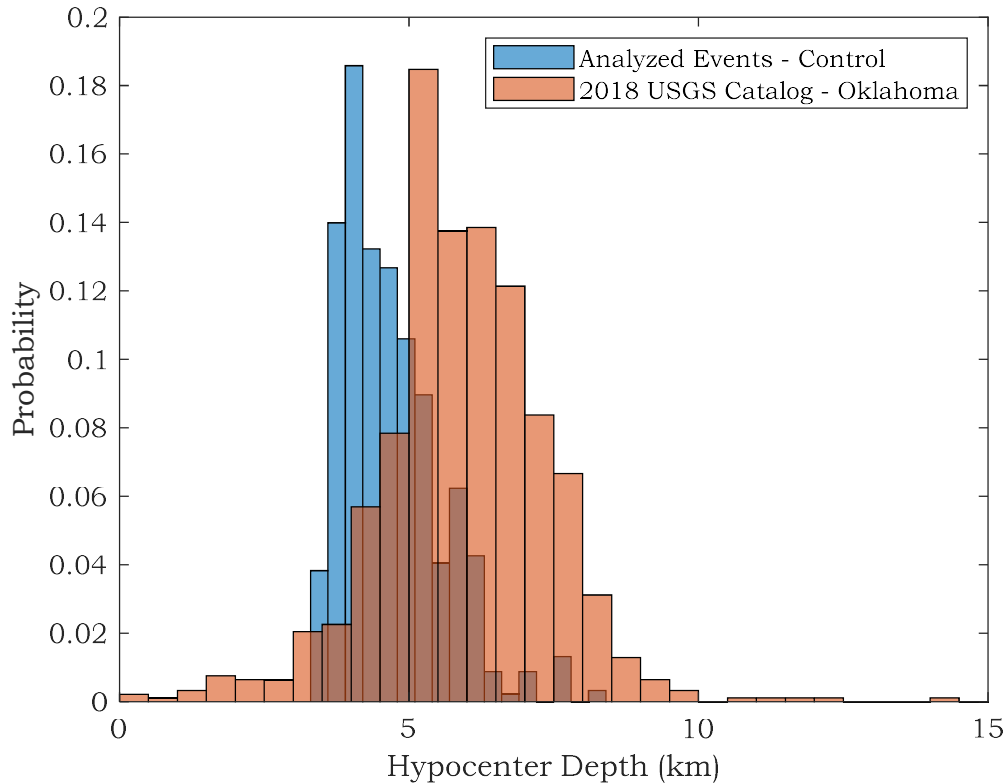
Figure 3-5 Histograms of USGS catalog (U.S. Geological Survey, n.d.) and model generated event depths

3.3.3 Limitations of the Hydromechanical Model

There are some limitations to this model. The one-dimensional basement column models represent an entire 1 km by 1 km section of the injection region. This may lead to over- or under-estimates of fluid pressure perturbation in plan for a column. The estimation errors are improved by reducing the area each column represents, so Haagenson considers as many columns as the

computer running the simulation allows. The loss of fluid to basement columns would have some effect on the pressure in the injection layer; for the injection layer, we assume that only a negligible amount of fluid flows into the much less permeable basement. The modeled subsurface is oversimplified by considering linear diffusion in a homogenous domain. We also ignore dynamic stress changes caused by injection, assuming induced seismicity is only triggered by changes in fluid pressure. These last two assumptions are common and often necessary in subsurface modeling (e.g. Brown et al., 2017; Dempsey & Riffault, 2019; Langenbruch et al., 2018).

Because the injection-level model is two-dimensional, all injection is assumed to occur at the same depth. This means that I cannot test the effect of changing injection depth as a mitigation strategy. With additional computing resources, I could use a true three-dimensional finite element model to simulate the effects of depth. This model also cannot consider fault properties and their relationship to earthquake magnitude. The magnitudes assigned by this model are randomly generated following a Gutenberg-Richter distribution.

3.4 Earthquake Magnitudes

For this study, I assume, as van der Elst et al. (2016) suggest, that induced earthquake magnitudes follow a Gutenberg-Richter magnitude-frequency distribution (Gutenberg & Richter, 1954). I have set the magnitude of completeness to $M_w2.0$. This is the lowest magnitude that will be generated.

This value was selected because the literature on triggering pressure for induced earthquakes is complete to this value (Goebel et al., 2017). I selected a *b* value of 1.0 for my theoretical site. Some locations of induced seismicity have higher or lower *b* values (e.g., Dempsey et al., 2016; van der Elst et al., 2016), but I am not trying to replicate a specific site.

The theoretical maximum magnitude for wastewater-injection-induced earthquakes is not yet well understood (Keranen & Weingarten, 2018). Some studies have suggested the upper limit on magnitude is dependent on injected volume (McGarr, 2014), while others suggest they follow the same patterns as tectonic earthquakes (van der Elst et al., 2016). I have selected a theoretical maximum magnitude of $M_w5.8$. Any earthquakes greater than this threshold are assigned to be $M_w5.8$. This is the magnitude of the largest known induced event and the cap of the earthquake catalog used in the ground motion prediction equation I use as the ground motion model (Zalachoris & Rathje, 2019). This assumption does not lead to a significant change in earthquake magnitude generation. In the control scenario, only 5 events out of a total 29,800 are large enough to be re-assigned to $M_w5.8$.

The weak points in the hydromechanical model are pre-seeded with magnitudes following the assumed Gutenberg-Richter distribution. Each run of the hydromechanical model will produce one earthquake catalog with earthquake event locations, time, and magnitudes following this distribution.

Uncertainty in magnitude is discussed in section 3.7.1. Fig. 3-6 shows the

distribution of the magnitudes generated for the control scenario.
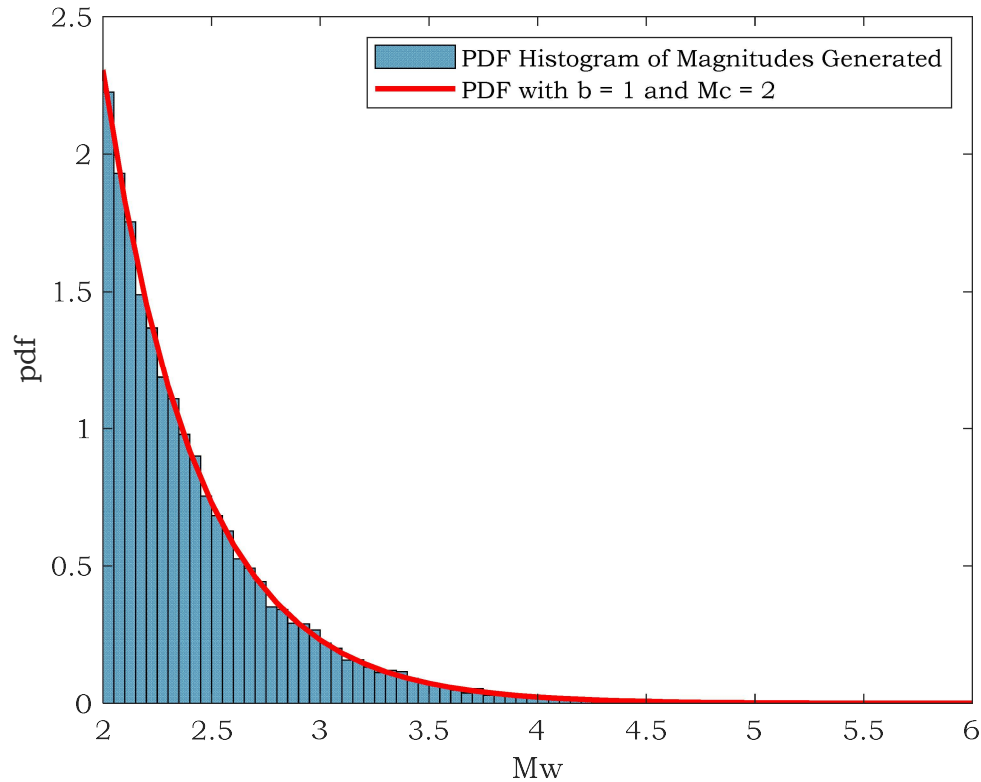
Figure 3-6 Histogram of all magnitudes generated in control case vs. target
probability distribution

3.5 Ground Motion Model

From the hydromechanical model and the associated magnitude

assumptions, I acquire earthquake location, time, and magnitude. Ground

motion intensities are generated for every earthquake with a magnitude over a

threshold. I use the Zalachoris and Rathje (2019) ground motion prediction

equation (GMPE) for small-to-moderate earthquakes in Texas, Oklahoma, and

Kansas, hereafter referred to as ZR19, to probabilistically generate ground

motion intensities over the region. At the time of this study, this is the most

recent GMPE for the region, including the largest catalog. A study that I have

expanded on, Baird et. al (2020) considered the Novakovic et al. (2018) GMPE

for the central and eastern United States. This GMPE gives similar intensity

outputs to ZR19 over the magnitude and distances considered in this study. I

analyze every earthquake over a magnitude threshold of $M_w3.5$ in my loss

model. I selected this threshold as Baird et al. (2020) found that at very short

distances between the earthquake and building, $M_w3.5$ earthquakes lead to a

nonzero probability of damage.

ZR19 takes inputs of hypocentral distance, earthquake depth, and

magnitude, as well as V_{s30} and fundamental period of the target structures. I

have selected a V_{s30} of 450 m/s for my region, as this is a typical value in

Oklahoma (Yong et al., 2016). A greater or lower V_{s30} would change my results

quantitatively, but not qualitatively. The model determines location parameters

by comparing the earthquake location from our hydromechanical catalogue to

the location of interest.

The GMPE outputs median ground motion intensities and residual

standard deviations. The ground motion parameters I produce are peak ground

acceleration (PGA) and spectral acceleration at the fundamental periods of both

building archetypes considered. The procedure for determining ground motion

intensity is outlined in Fig. 3-7.
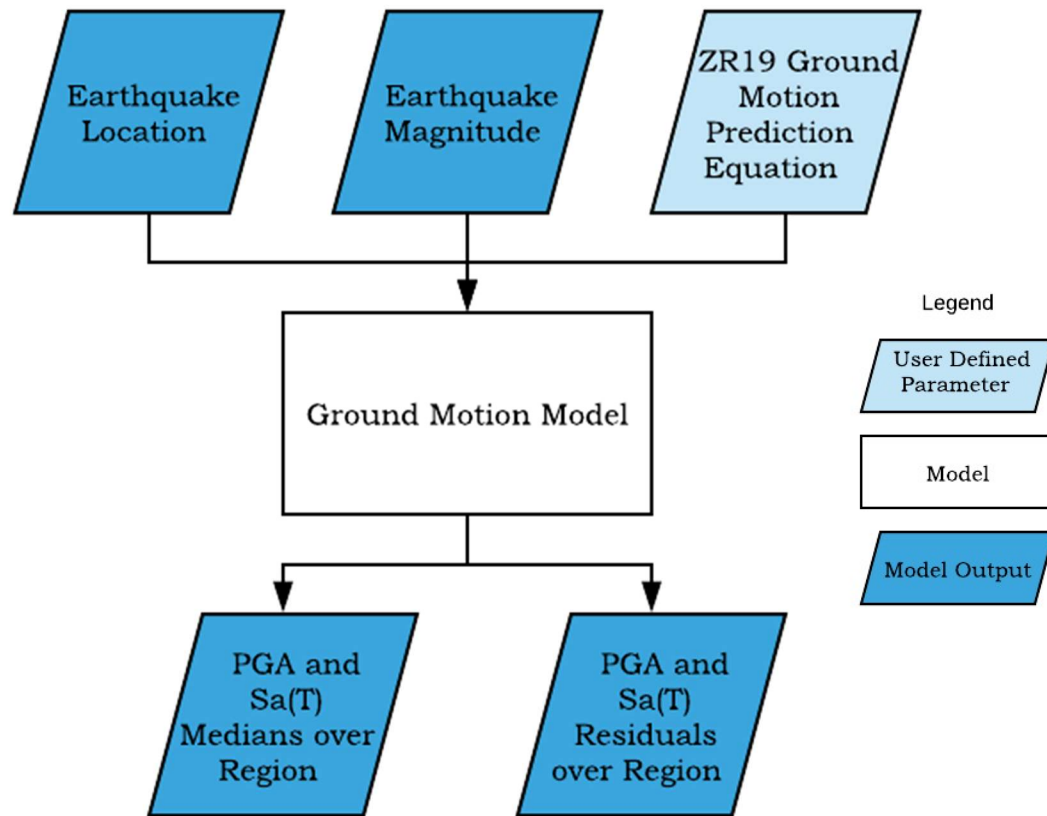
Figure 3-7 Flowchart of ground motion model

Ground motion intensities are quantified at 1 km spacing over the entire study region, for a total of 14,400 sets of x and y coordinate pairs, each with intensity values for a ground motion realization. Uncertainty in ground motion, including spatial correlations, is discussed in section 3.7.2.

3.6 Loss Model

The loss model takes in ground motion intensities from the previous step, vulnerability or loss curves for buildings of interest, and locations of buildings of interest. The procedure for determining loss in terms of repair cost

is outlined in Fig. 3-8. The definition of the archetype buildings of interest, and the creation of loss curves is discussed in section 3.6.1 and the creation of the archetypal towns and region is discussed in section 3.6.2.

For individual buildings, I consider single-family dwellings (SFD) and multi-family dwellings (MFD). The loss to a single building at any location is determined by comparing the ground motion determined in the previous step to the loss curve for that building (developed as described below). Loss to each building archetype is found at 1 km spacing over the entire study region, at the locations where I have determined ground motion intensity. This leads to 14,400 loss values over the region for a given realization.

I have produced three archetypical towns to consider loss to a community. Using the same methodology as for an individual building at any location, I determine loss for each building in the inventory independently and sum the losses to determine community loss. I have also designed an archetypal region with 35 towns of the three archetypes to simulate earthquake loss to the entire region. Uncertainty in loss is discussed in section 3.7.3.
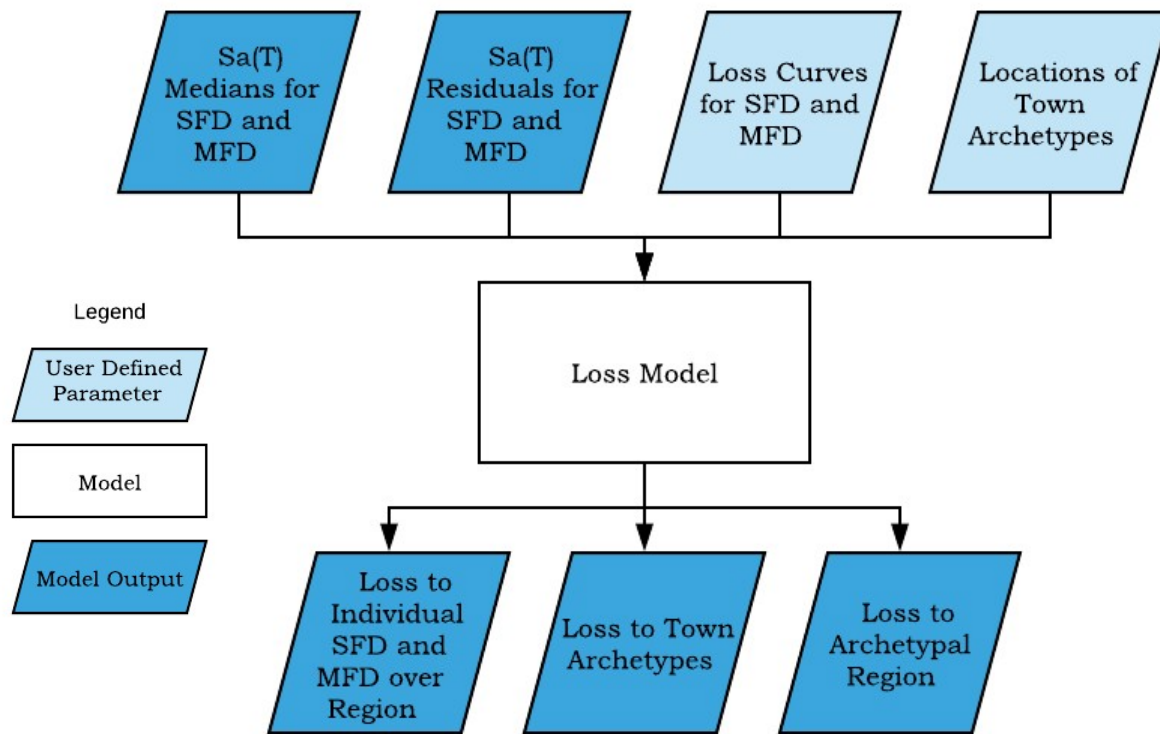
Figure 3-8 Flowchart of loss model

3.6.1 Loss Curves for Archetype Buildings

A SFD and a MFD are the two buildings considered in this study. These light frame wood buildings, reviewed by professional engineers, were originally designed for ATC 116 to follow ASCE 7-10 with Seismic Design Category C for moderate seismicity (ATC, 2019). Both buildings were redesigned for Seismic Design Category B to better represent the recent building stock of the CUS (Baird et al., 2020). These buildings are modern construction and may perform better than older buildings in the region. Older buildings may have deterioration in some structural components. The buildings are shown in Figs.

3-9, 3-10, 3-11, and 3-12 below. The SFD has a replacement cost of $528,000 and the MFD has a replacement cost of $1,622,000.
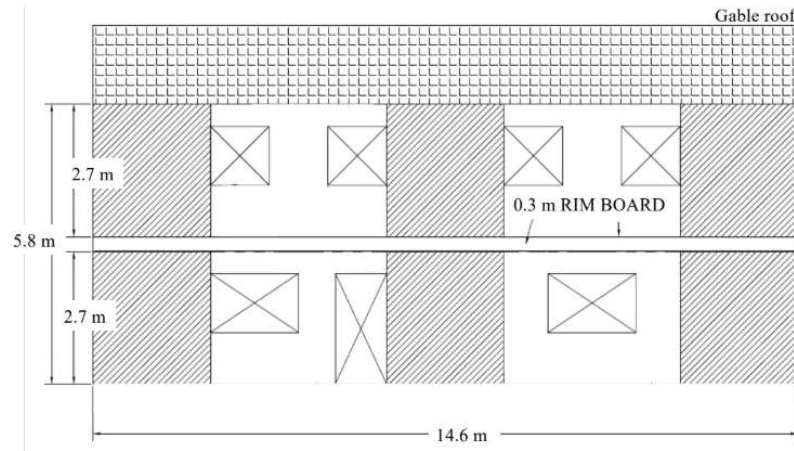
Figure 3-9 Elevation view of SFD archetype used in this study (Baird, 2019)
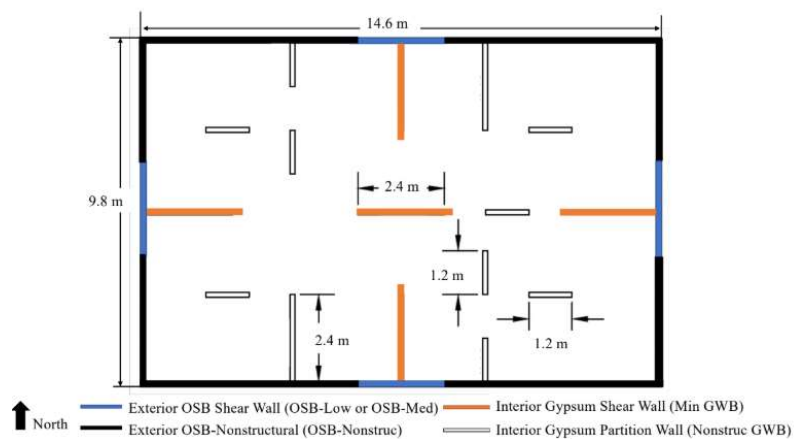
Figure 3-10 Plan view of SFD archetype showing shear and bearing wall layout (Baird, 2019)
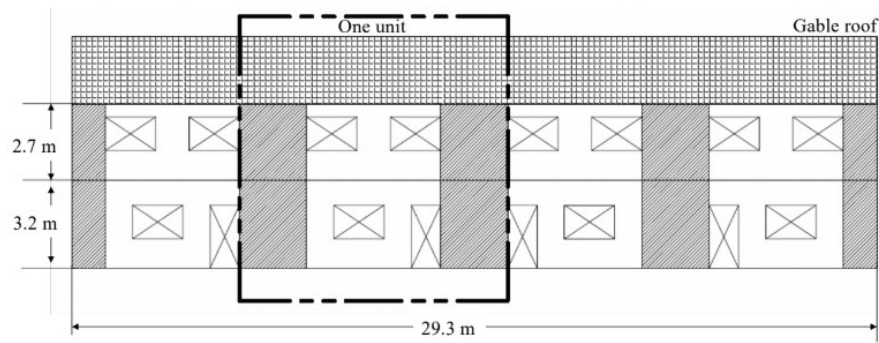
Figure 3-11 Elevation view of MFD archetype used in this study (Baird, 2019)
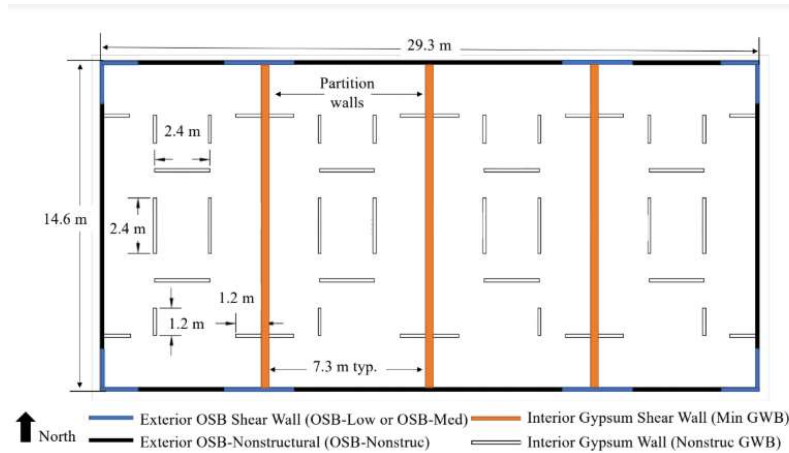
Figure 3-12 Plan view of MFD archetype showing shear and bearing wall layout (Baird, 2019)

The SFD has a fundamental period of 0.32 seconds and the MFD has a fundamental period of 0.48 seconds. These buildings were modeled in 3D by Baird et al. (2020) in Timber3D, with nonlinear behavior in wall elements, in order to simulate structural response to earthquake motions. Baird et al. (2020) considered 68 ground motions selected from the Assatourians & Atkinson (2020) database of induced earthquake motions from Oklahoma, US

and Alberta, CA. Baird et al. (2020) scaled these motions to match frequency and intensity of various, potentially-damaging target scenarios for induced seismicity in the central U.S.. This analysis produced story drift and floor acceleration values at various levels of ground motion. The intensity measure of interest was spectral acceleration at the fundamental period of the structure.

I used another program, the Seismic Performance Prediction Program (SP3), to determine loss values from story drift and floor accelerations using FEMA P-58 methodology (Haselton & Baker, n.d.). The FEMA P-58 methodology is an assembly-based loss estimation procedure that quantifies damage to structural and nonstructural components, based on predefined fragilities. The methodology links these component damage states to repair actions and costs. Repair costs are the sum losses to the components in the building, and the analysis is fully probabilistic (FEMA, 2018).

To use the SP3 implementation of FEMA P-58, I input site information (seismic design category, site class, and location), building components and quantities, and the Baird et al. (2020) structural responses into the program. SP3 uses my inputs and the FEMA P-58 fragility database to run a FEMA P-58 Monte Carlo analysis. The result is a loss or repair cost vs. ground motion intensity curve for each building, as shown in Figs. 3-13 and 3-14. If the ground motion exceeds where the intensity range over which the loss curve has been developed, the final loss value is extended with zero slope to avoid overestimating loss. This may underestimate loss, but across the region,

considering all earthquakes, the SFD threshold was exceeded in 0.0008% of the calculations and the MFD threshold was exceeded in 0.0006% of the calculations. Therefore, this assumption does not make a great difference.
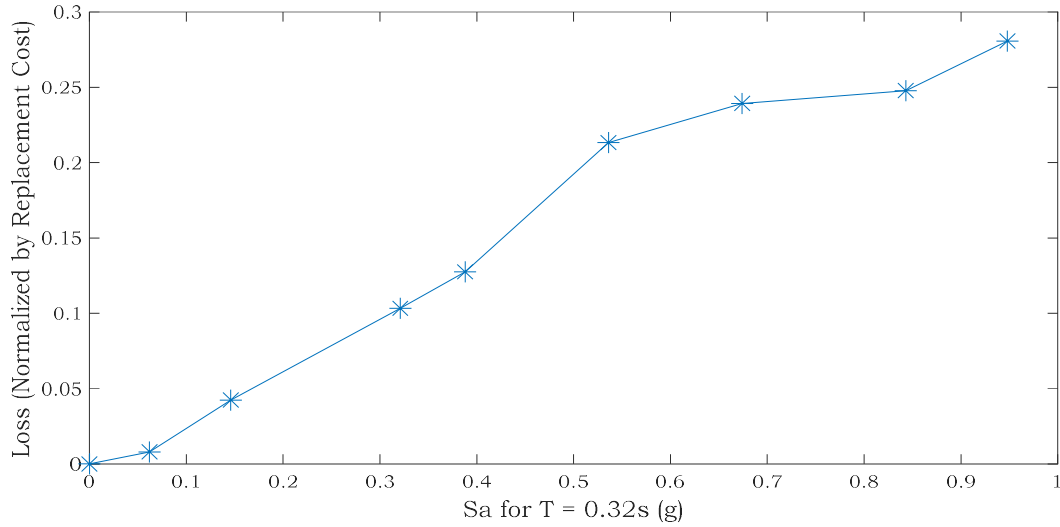
Figure 3-13 Economic losses or repair costs, conditioned on ground motion intensity, for SFD
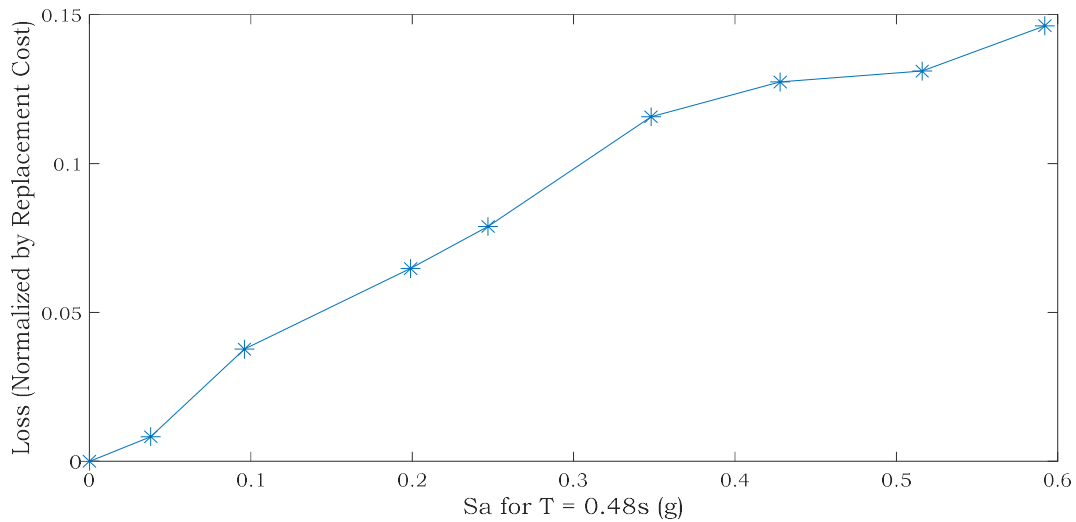
Figure 3-14 Economic losses or repair costs, conditioned on ground motion intensity, for MFD

3.6.2 Archetypal Towns

Three archetypal towns were designed in order to assess loss to a group of structures. The key details of each town are outlined in Table 3-2.

Table 3-2 Details of archetypal towns

Town Name	Population	Household Count	Percent in MFD	SFD Count	MFD Count
Farmington	250	97	10%	87	3
Middlesville	2525	979	40%	587	70
Smalltown City	7700	2985	55%	1343	164

Using census data, the average household sizes of Kansas, Oklahoma, and Texas are 2.52, 2.58, and 2.86 respectively (*QuickFacts: Texas; Kansas; Oklahoma,* 2018). For determining the number of buildings per town archetype, I selected the median value of 2.58 persons per household. The percentages of families in multi-family housing assumes that larger percentages of households occupy MFDs in the larger towns.

For analysis purposes, each town is placed at three locations and assessed for damage. I consider a town in the center of the injection region, a town 20 km from the edge of the injection region, and a town 50 km from the edge of the injection region as shown in Table 3-3, all with a constant y-distance component. I have also plotted these locations on Fig. 3-2.

Table 3-3 Locations of archetypal towns for individual loss analysis

Town Location	X Coordinate (km)	Y Coordinate (km)
Center of injection region	60	60
20 km from edge	30	60
50 km from edge	1	60

Additionally, an archetypal region was created, emulating a region in rural Northern Oklahoma and Southern Kansas. Oklahoma and Kansas have population densities of 21.1 and 13.5 people per square kilometer, respectively (*QuickFacts: Texas; Kansas; Oklahoma*, 2018). This population density includes high-density urban areas, so I am considering a slightly lower density for my rural region. I first designed a road network and then located towns near intersections. I placed a road bisecting the region to emulate an interstate. From this road, I placed tributary roads, simulating state highways coming from the interstate and county roads to reach more remote areas of the region. Town placement is roughly size correlated, with large towns having medium towns nearby and small towns further away. To reach a realistic population density, I include three large towns, thirteen medium towns, and nineteen small towns in the region. This leads to a population density of 4.2 people per square kilometer (10.8 people per square mile) across the entire region. For context, 18 of the 77 counties in Oklahoma and 56 of 105 counties in Kansas have population densities lower than this value (*QuickFacts: Texas; Kansas; Oklahoma*, 2018). This region is depicted in Fig. 3-15. This region is not intended to represent a specific location and any similarities are coincidental. I

determine loss for each injection scenario across this entire region by summing the losses from each town.
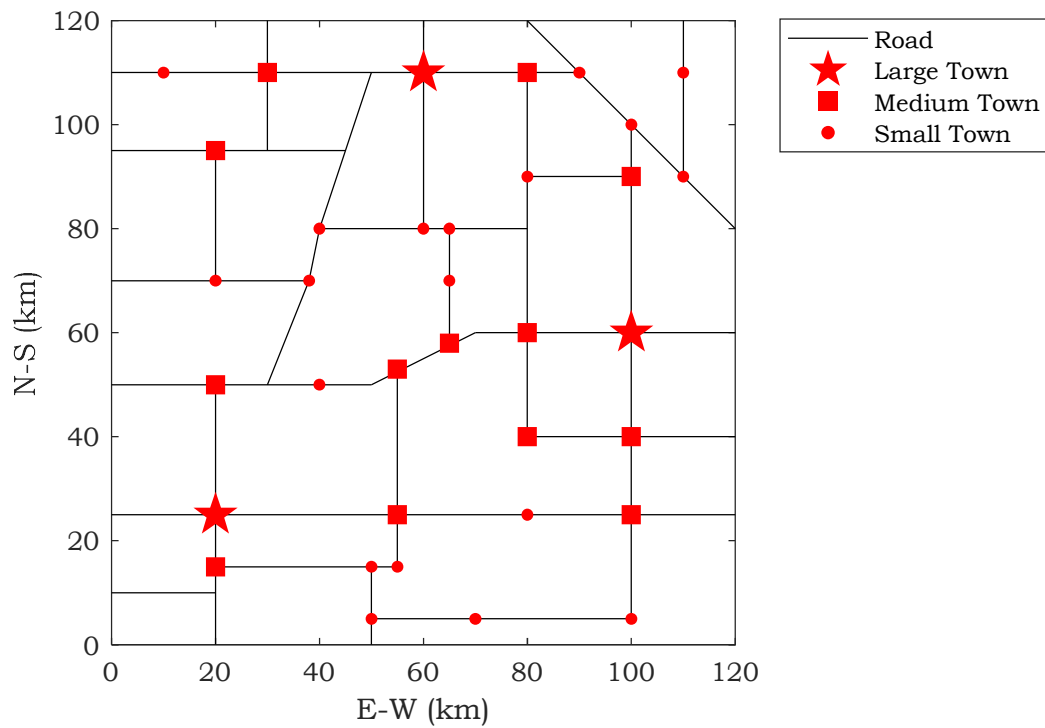
Figure 3-15 Archetypal region

3.7 Uncertainties

There is uncertainty in these steps that must be considered. These quantities are magnitude, intensity, and loss. Uncertainties are propagated through the analysis with Monte Carlo simulation.

3.7.1 Uncertainty in Magnitude

Each magnitude is randomly generated following the Gutenberg-Richter distribution (Fig. 3-6). To propagate the uncertainties in magnitude generation, I reassign magnitudes several times following the same distribution. To determine the number of times magnitude needs to be re-assigned, I produce 300 earthquake catalogs by reassigning magnitude. I then calculate the mean magnitude and the sum of all magnitudes for each of the 300 catalogs. The mean is a measure of central tendency and the sum of the magnitudes can be considered a proxy for expected loss in a catalog. I find the standard deviation of these values considering any number of catalogs, by taking the values of mean and sum magnitudes from each of the first catalogs up to that number. At the point where the plots of standard deviation cease to change by adding another catalog, the uncertainty has been captured to a reasonable degree. This point appears to be around realization 50. I choose to consider 100 realizations of magnitude to expand the dataset. Fig. 3-16 outlines the procedure for determining the number of catalogs needed.
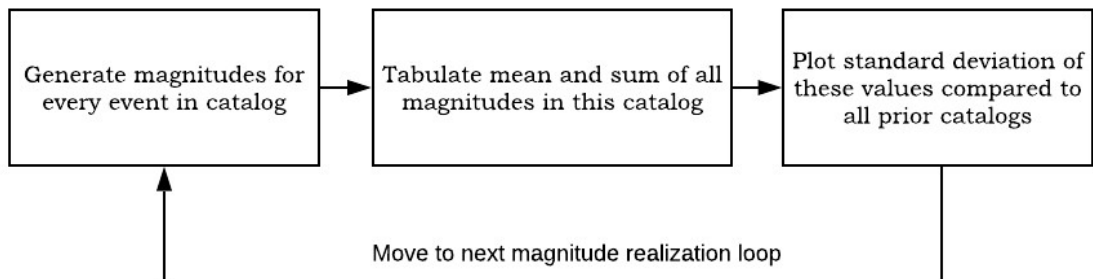
Figure 3-16 Flowchart of magnitude uncertainty procedure

3.7.2 Ground Motion Intensity Uncertainty

ZR19 gives standard deviation values for inter- (between) and intra-(within) event residuals. For a given earthquake, the inter-event residual is a constant for all sites for a specific period, while the intra-event residual represents spatial correlation between sites (Loth & Baker, 2013). Both types of residual exhibit correlations between different fundamental periods. I have followed the procedure outlined by Baker and Jayaram (2008) to randomly generate inter-event residuals correlated to the considered fundamental periods. I have followed the procedure outlined by Loth and Baker (2013) to randomly generate intra-event residuals correlated in space and to the considered fundamental periods. I combine the median ground motion intensity with randomly generated residuals to find a realized ground motion intensity.

To determine the amount of times ground motion intensity needs to be realized, I produce 300 maps of ground motion intensity for the region by re-generating random residuals for one earthquake. I then calculate the mean intensity and the maximum intensity over the region for every earthquake realization. I find the standard deviation of these values considering any number of realizations by taking the values of mean and maximum intensity from each of the first catalogs up to that number. At the point where the plots of standard deviation cease to change by adding another realization, the uncertainty has been captured to a reasonable degree. Again, I choose to

consider 100 realizations of ground motion intensity. Fig. 3-17 outlines the procedure for determining the number of realizations needed.
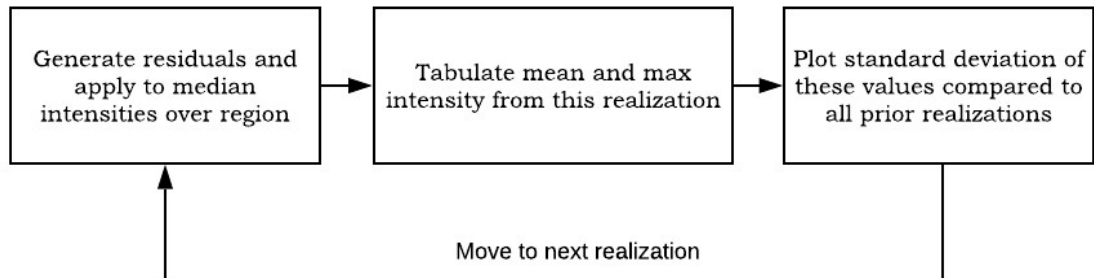
Figure 3-17 Flowchart of ground motion intensity uncertainty procedure

3.7.3 Loss Uncertainty

With SP3, I run a Monte Carlo simulation with 10,000 realizations of building and component loss at each of nine levels of ground motion intensity. Uncertainties in repair costs or losses conditioned on ground motion intensity are determined from SP3, which propagates uncertainties in component damage and repair costs by taking random realizations for analysis. I order the SP3 loss realizations by rank at each inputted ground motion intensity. The loss model selects a random loss realization index from 1 to 10,000 (total number of realizations) and interpolates over the ground motion intensity at a location to find the realized loss for a building at that location. This method accounts for the fact that greater losses are expected in locations of greater ground motion intensity, but there could be some variability from construction materials or techniques.

With the uncertainty in loss conditioned on intensity in hand, uncertainties in losses could be considered two ways. Loss can be realized a number of times for every individual intensity realization, or losses could be realized single time for each intensity realization. To test, I first produce 300 ground motion intensity maps. I consider both 100 realizations of loss at each site for every intensity realization and a single realization of loss at each site for every intensity realization. I then calculate the mean loss and the maximum loss over the region for every ground motion realization. When considering 100 loss realizations on each ground motion realization, there is an extra step. I find the mean loss and maximum loss for a location independently for each loss realization for a given ground motion intensity and take the median value over the 100 realizations to find the mean and maximum loss values for that ground motion realization intensity. I find the standard deviation of these values considering any number of ground motion realizations by taking the values of mean and maximum losses from each of the first realizations up to that number. At the point where the plots of standard deviation cease to change by adding another realization, the uncertainty in loss has been captured to a reasonable degree.

Both methods need about 100 loss realizations for standard deviation to stabilize when adding additional realizations. I also found that a single loss realization per each ground motion realization gave a very similar value to multiple loss realizations per ground motion realization. From this, I decide to realize loss a single time on each of the 100 ground motion realizations, in

order to produce 100 loss realizations. Fig 3-18 outlines the procedure for

determining the number of realizations needed given one loss realization for

each ground motion intensity.
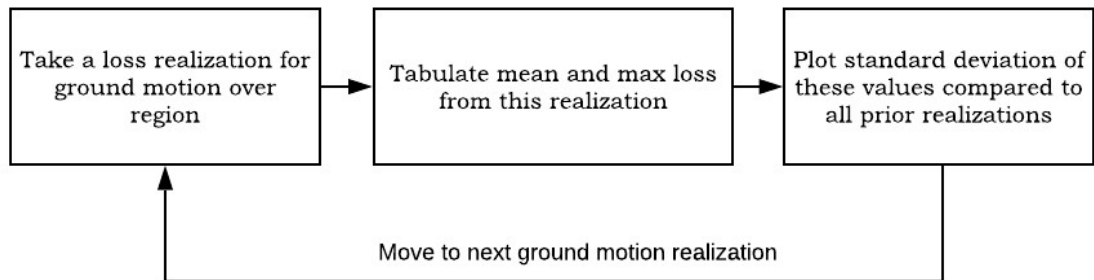
Figure 3-18 Flowchart of loss uncertainty procedure assuming one loss
realization per ground motion realization

3.8 Mitigation Scenarios

I consider three types of mitigating actions, and varying levels of each.

These are: increased spacing between injection wells, an overall reduction in

injection volume, and a traffic light system. My control scenario is 16 wells,

spaced on a grid evenly at 3 km as shown in Fig. 3-19.
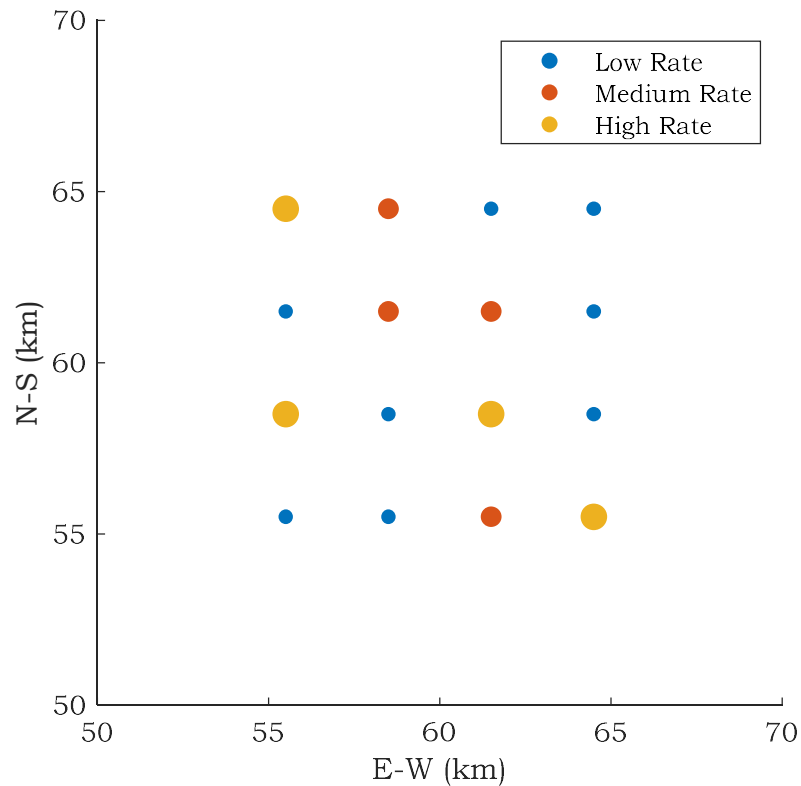
Figure 3-19 Control scenario well locations within the 20 km x 20 km bounds of the hydromechanical model

For alternative spacings, I consider well locations randomly generated following a uniform distribution, 4 km grid spacing, and 5 km grid spacing. The grid spacing was selected for simplicity. The randomly generated well locations case represents a more realistic injection region and is intended to validate that my grid spacing gives realistic earthquake distributions. The randomly generated well locations have an average minimum spacing of 2.4 km.

For the overall reduction scenarios, I am considering three levels of reduction: 25%, 40% as mandated by the OCC (Skinner, 2016a, 2016b), and 50%. I am considering two cases of each. The first case, "perpetual reduction",

assumes six months at base injection levels to prime the model followed by 18 months of reduced injection. The second, "cycled reduction", considers a reduction that is cycled on and off. I run the simulation with six months at base injection levels, followed by six months of reduced injection, and repeat this pattern for a second year. The control, spacing, and reduction cases are outlined in Table 3-4. Fig. 3-20 shows the cumulative injection over time from perpetual reduction scenarios and Fig. 3-21 shows the cumulative injection over time from the cycled reduction scenarios.

Table 3-4 Control, spacing, and reduction cases

Case	Number of Wells	Spacing (km)	Injection Rate 1 (m^3/hr)	Well Count at Rate 1	Injection Rate 2 (m^3/hr)	Well Count at Rate 2	Injection Rate 3 (m^3/hr)	Well Count at Rate 3
Control	16	3	0.5	8	3	4	55	4
S1 - Random	16	-	0.5	8	3	4	55	4
S2 - 4km Spacing	16	4	0.5	8	3	4	55	4
S3 - 5km Spacing	16	5	0.5	8	3	4	55	4
R1 - 25% - Perpetual	16	3	0.375	8	2.25	4	41.25	4
R2 - 40% - Perpetual	16	3	0.3	8	1.8	4	33	4
R3 - 50% - Perpetual	16	3	0.25	8	1.5	4	27.5	4
R4 - 25% - Cycled	16	3	0.375	8	2.25	4	41.25	4
R5 - 40% - Cycled	16	3	0.3	8	1.8	4	33	4
R6 - 50% - Cycled	16	3	0.25	8	1.5	4	27.5	4
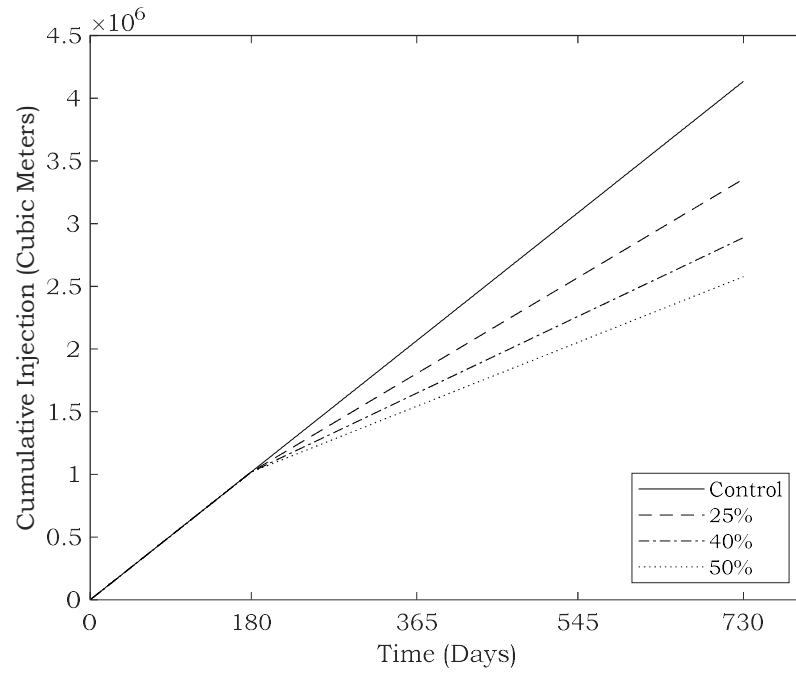
Figure 3-20 Cumulative injection vs. time for perpetual reduction cases
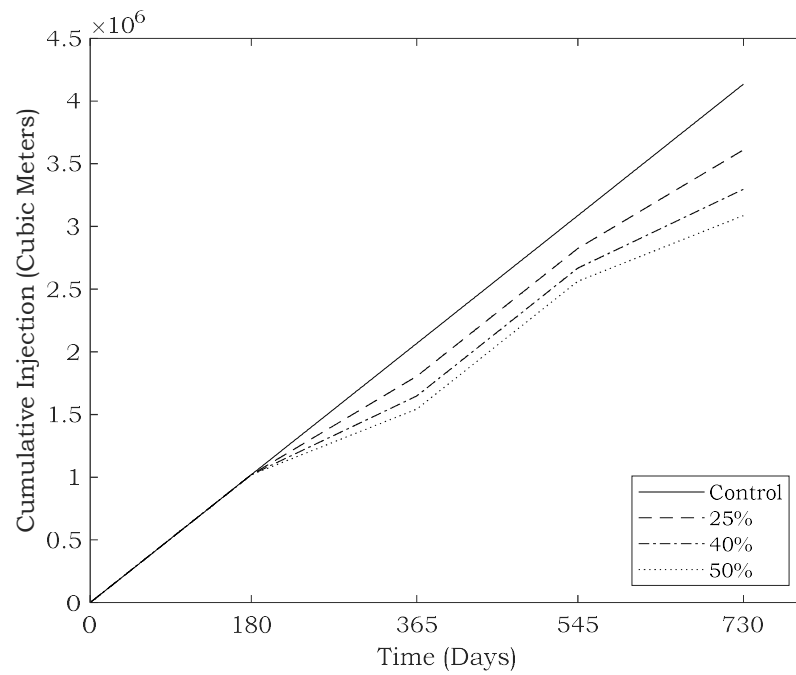
Figure 3-21 Cumulative injection vs. time for cycled reduction cases

I also look at several different combinations of traffic light thresholds and actions, shown in Table 3-5. For the traffic light cases, a radius of 5 km was defined around all the wells. Oklahoma requires seismicity review to obtain a "yellow light permit" for any operations within 3 miles (about 5 km) of a stressed fault (T. Baker, 2015). All wells begin our simulation in a green-light condition. This condition implies that earthquakes are nonexistent or small enough to not be of concern or not detectable (Kao et al., 2016). A well goes to yellow-light condition when seismicity begins to increase and is typically associated with some modification of injection operations or an increase in monitoring (Kao et al., 2016). If a yellow-light event occurs within the 5 km radius of a well, the yellow-light action adjusts the well operations, through the action listed in the table. If a second yellow-light event occurs while the well is in a yellow-light condition, the well is upgraded to a red-light status. A red-light threshold is usually assigned to either the magnitude threshold at which damage is expected or a more conservative magnitude to limit future, more damaging events (Kao et al., 2016). If a yellow- or red-light earthquake event occurs while the well is in a red-light condition, the red-light timer is reset. To compare the TLS cases to the injection reduction cases, in my scenarios, the traffic light becomes active after six months (180 days).

Table 3-5 Traffic light system cases

Case	Yellow Threshold (Mw)	Yellow Action	Red Threshold (Mw)	Red Action
TLSC	2.5	Operate at 50% volume for 28 days	3.5	Stop for 28 days
TLS1	2.5	Operate at 50% volume for 56 days	3.5	Stop for 56 days
TLS2	3	Operate at 50% volume for 28 days	3.5	Stop for 28 days
TLS3	2.5	Operate at 50% volume for 28 days	4	Stop for 28 days
TLS4	2.5	Operate at 75% volume for 28 days	3.5	Stop for 28 days
TLS5	3	Operate at 50% volume	3.5	Stop
TLS6	2.5	Operate at 50% volume	4	Stop
TLS7	2.5	Operate at 75% volume	3.5	Stop
TLS8	2	Operate at 50% volume for 28 days	3	Stop for 28 days

I consider 9 different traffic lights, considering permutations on magnitude thresholds or reactions. These traffic lights range in how aggressively they reduce cumulative injection rates. The lower magnitude threshold traffic lights will be triggered earlier. The traffic lights with a red-light mandating that injection must cease for perpetuity likely lead to significantly lower total injection volumes. The base traffic light (TLSC) is designed to be generic, with a yellow-light threshold of $M_w2.5$. To reach this detection threshold, I assume this operation will have some seismic monitoring capability to improve the detection threshold, as there is a $M_w3.0$ detection threshold of most of the United States (McGarr et al., 2015). I define my red-light threshold low enough here to try to prevent larger, damaging earthquakes. I have chosen

both actions to be applied for one month. I expect one month to be long enough for the system to respond to the decreased or ceased injection.

4 Results

4.1 Hydromechanical Model

4.1.1 Pressure Perturbations

The hydromechanical model takes in parameters of injection rates and locations as well as hydraulic properties of the region in order to model pressure diffusion as a result of injection operations. Fig. 4-1 shows how pressures diffuse from the injection locations in two-dimensional space for the control scenario and various mitigation cases. Contours are overlain at 0.01 MPa and 0.1 MPa to represent the range of triggering pressures considered. These contours are helpful to show the two-dimensional pressure perturbation, but it does not mean a weak point within a contour has triggered. Pressure must also diffuse downward to the location of the weak point before it can trigger.

The low-rate wells have greater pressure perturbations when they are located closer to high-rate wells. In the control case, the area around the low-rate well in the bottom left (adjacent to a high-rate well) reaches the minimum triggering threshold of 0.01 MPa by the 180 (Fig. 4-1a) day plot. However, in the same case, the low-rate well in the top right (injecting at the same rate, but located further from high-rate wells) does not reach the 0.01 MPa in the 180 (Fig. 4-1a) or 365 (Fig. 4-1b) day plots plot. The delay occurs because of the less significant interactions between wells.
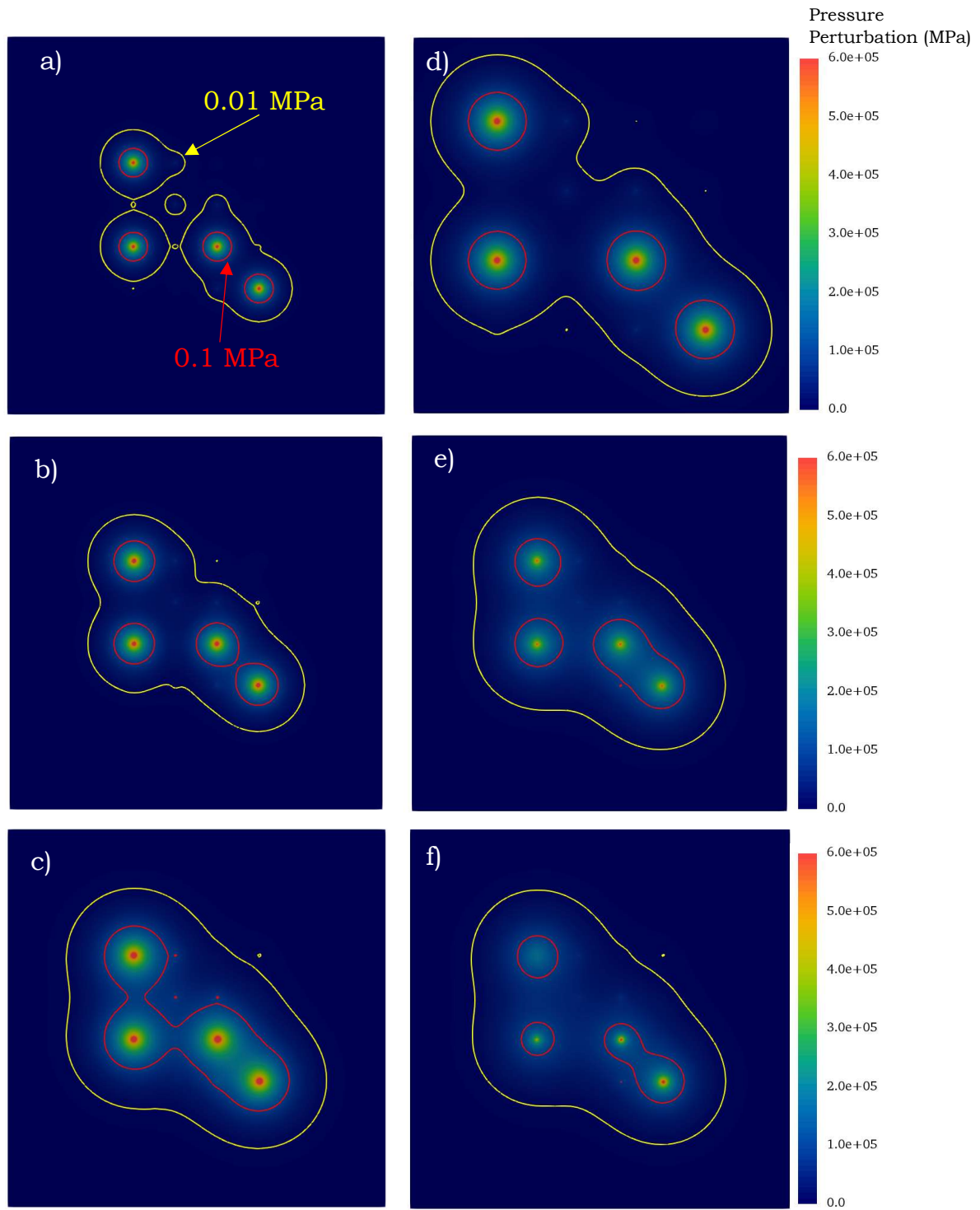
Figure 4-1 Pressure perturbations from hydromechanical model over 20 km x 20 km region

a) Control scenario at 180 days, b) Control scenario at 365 days, c) Control scenario at 730 days, d) 5 km spacing (S3) at 730 days, e) 40% injection reduction (R2) at 730 days, f) Base TLS (TLSC) at 730 days

To represent all three mitigation strategies, I have shown plots for well spacing increased from 3 km to 5 km (S3, Fig. 4-1d), injection reduced by 40% (R2, Fig. 4-1e), and the control traffic light (TLSC, Fig. 4-1f), each at 730 days. When comparing the mitigation scenarios to the control scenario at 730 days (Fig. 4-1 c), the area enclosed by 0.01 MPa contours is not greatly reduced. In fact, the increased well spacing case (Fig. 4-1d) extends the 0.01 MPa boundary. This trend occurs because increasing well spacing moves wells radially outward from the center and wells are now closer to the boundaries of the modeled injection region. The 0.1 MPa contours in all the mitigation cases considered, however, are much less extensive. Therefore, the faults with lowest triggering pressures (perhaps because they are optimally oriented) may trigger even with mitigating actions, but the mitigating action should prevent many of the less optimally-oriented faults from triggering, reducing overall seismicity in the region.

4.1.2 Earthquake Generation

When the pressure perturbation at a weak point location reaches the triggering pressure for that weak point, an earthquake occurs. Fig. 4-2 shows all earthquake locations in two dimensions for the control scenario with contours overlain at 0.01 MPa and 0.1 MPa of pressure perturbation to compare the spatial extents of the earthquakes to the pressure perturbation of the control scenario at 730 days. The area within the 0.1 MPa contour has many events, the area of the 0.01 MPa contour has fewer, and there are none outside of this region. Fig. 4-3 shows the same data (without the pressure

perturbations) in three dimensions, such that the additional effect of depth is apparent. We see many earthquakes in the top few kilometers of the crystalline basement. This trend is partly due to weak point distribution being skewed toward more shallow events, and partly due to pressure perturbations not extending as far down into the one-dimensional models of the basement rock.
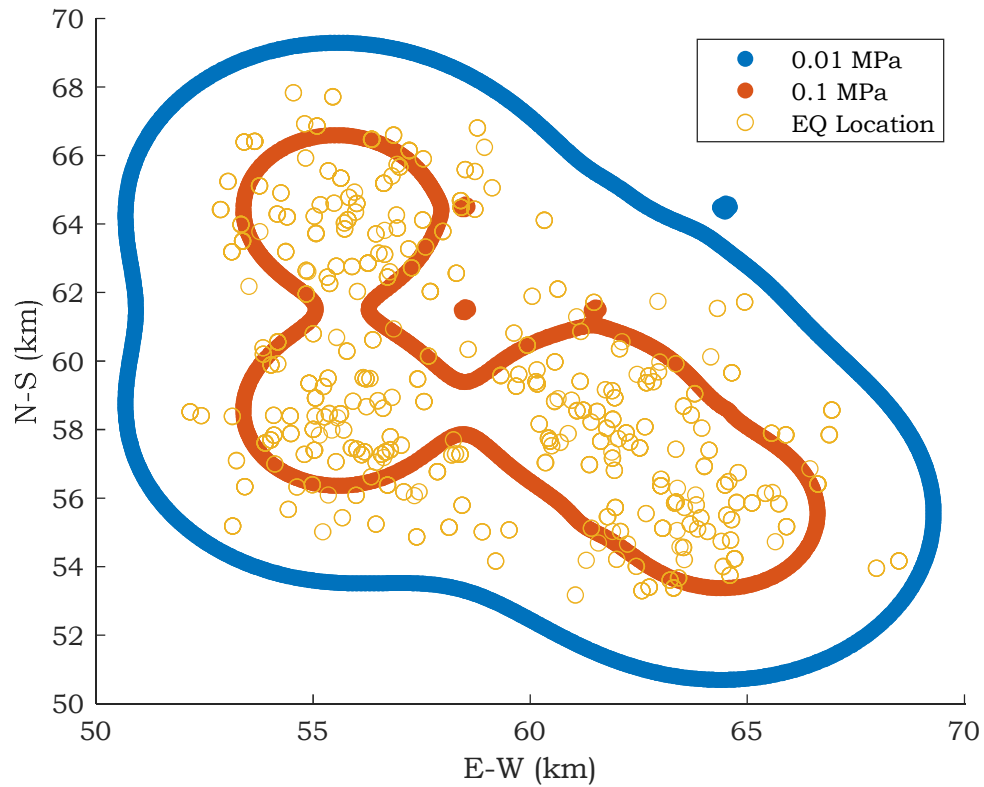
Figure 4-2 Location of all earthquake events in two dimensions in the control scenario with triggering pressure contours
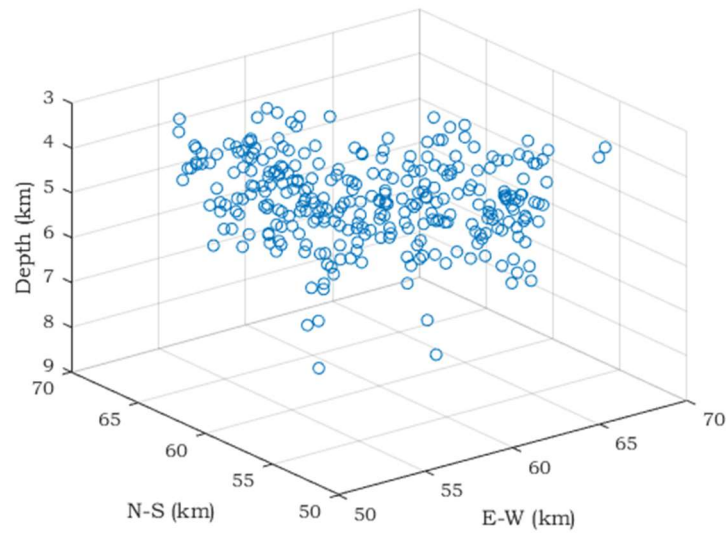
Figure 4-3 Location of all earthquake events in three dimensions in the control scenario

4.1.3 Earthquake Occurrence

A full breakdown of earthquake counts and injected volume, broken down to six-month intervals, can be found in Table 4-1.

Table 4-1 Earthquake count and injected volume, 6-month intervals, all cases

Scenario	0:182 Days		183:365 Days		366:547 Days		548:730 Days		Total	
	Volume (10^6 m³)	EQ Count	Volume (10^6 m³)	EQ Count	Volume (10^6 m³)	EQ Count	Volume (10^6 m³)	EQ Count	Volume (10^6 m³)	EQ Count
Control	1.03	46	1.04	60	1.03	86	1.04	106	4.13	298
S1	1.03	28	1.04	62	1.03	77	1.04	89	4.13	256
S2	1.03	27	1.04	53	1.03	84	1.04	99	4.13	263
S3	1.03	33	1.04	54	1.03	66	1.04	77	4.13	230
R1	1.03	46	0.777	57	0.773	70	0.777	85	3.36	258
R2	1.03	46	0.622	57	0.619	56	0.622	77	2.89	236
R3	1.03	46	0.518	56	0.515	44	0.518	74	2.58	220
R4	1.03	46	0.777	57	1.03	74	0.777	92	3.61	269
R5	1.03	46	0.622	57	1.03	62	0.622	89	3.30	254
R6	1.03	46	0.518	56	1.03	56	0.518	88	3.09	246
TLSC	1.03	46	0.542	56	0.508	54	0.374	63	2.46	219
TLS1	1.03	46	0.242	54	0.307	35	0.226	50	1.81	185
TLS2	1.03	46	0.897	60	0.807	80	0.827	90	3.56	276
TLS3	1.03	46	0.542	56	0.508	54	0.374	63	2.46	219
TLS4	1.03	46	0.536	58	0.430	55	0.379	64	2.38	223
TLS5	1.03	46	0.837	60	0.262	71	0.00110	57	2.13	234
TLS6	1.03	46	0.211	53	0.00437	31	0.00281	17	1.25	147
TLS7	1.03	46	0.211	55	0.00437	30	0.00240	25	1.25	156
TLS8	1.03	46	0.133	50	0.253	28	0.140	30	1.56	154

For the well spacing cases (Fig. 4-4), the mitigating action is effective at day 0 because increased well spacing is a strategy intended for a new injection region. Even with equal injection volumes to the control case, increased well spacing has a significant effect on the number of earthquakes generated in a two-year period, leading to reductions up to 23% in earthquake count for the 5 km spacing case. Interestingly, the randomly generated well locations case (S1) and the 4 km spacing case (S2) follow very similar trends to each other when comparing earthquake count vs. time. Even though the random spacing has a much lower minimum distance between wells (1.21 km), both cases have very similar average spacing between injection wells. The random spacing case has an average distance of 8.09 km between any two wells and the 4 km minimum spacing case has an average distance of 8.56 km between any two wells. It appears that the average distance between injection wells might be more important than the minimum distance, but a much larger sample size of analysis cases would be needed to prove this hypothesis.

The wider 5 km spacing case (S3) sees more earthquakes than the 4 km spacing case (S2) through the first year, but significantly fewer in the second year. I hypothesize that this is because a larger area of the injection region sees some degree of pressure perturbation, leading to more initial earthquakes. As time elapses, the well-to-well interactions begin to have more influence and the tighter spaced wells see greater earthquake rates.
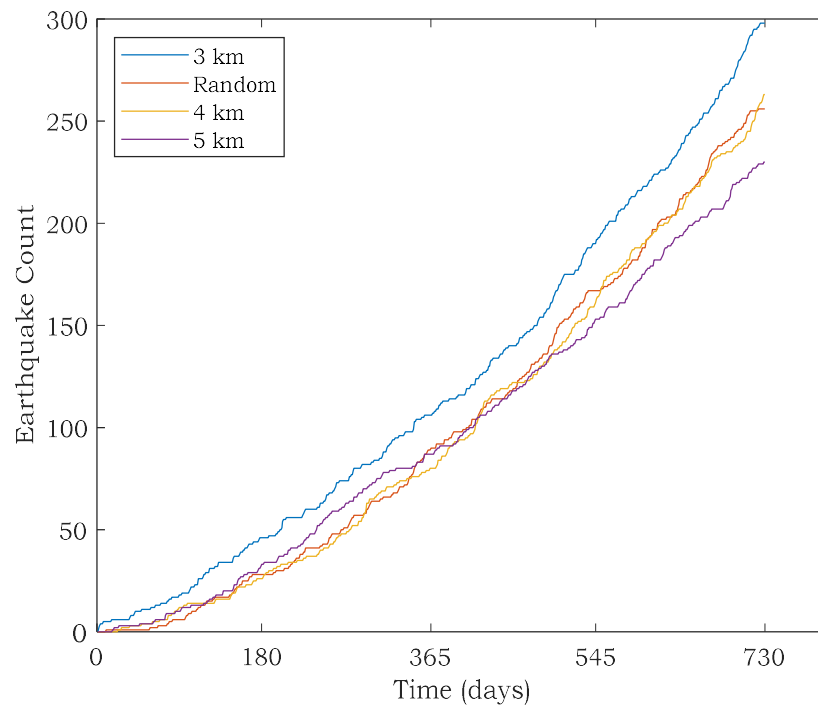
Figure 4-4 Earthquake count vs. time, considering mitigation strategies with alternate well spacing

Fig. 4-5 compares the reduction cases to the traffic light cases. Both of these strategies change only injection levels and no other model properties. I have plotted a trendline for the traffic light cases. From this trendline, my TLS cases expect about an additional 57 earthquakes above M_w2 (the magnitude of completeness for my magnitude distribution) for every million cubic meters of injectate in this region. I have normalized this slope for simplicity because of the large volumes considered in this study. This slope is sensitive to model parameters; changing the layer properties will lead to more or fewer earthquakes so this value should not be used for justifying a new policy. Cases falling above this line are less efficient than average in terms of injection

volume, meaning they reduce injection volume without as strong of a reduction in earthquakes, while cases falling below are more efficient than average. Each of the six overall reduction cases fall below this line, meaning, on an average sense, overall reduction is more efficient than traffic light systems. The reduction cases all produce less earthquakes than expected given the TLS trend.
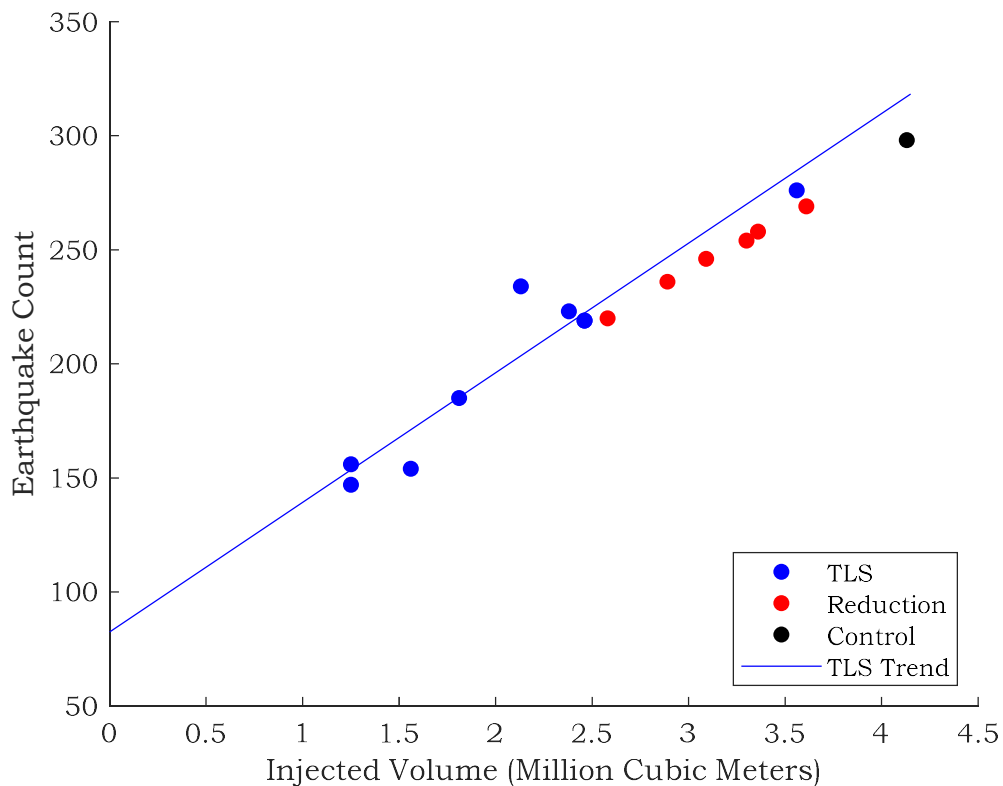
Figure 4-5 Comparison of traffic light system and overall reduction cases at 730 days

For the injection reduction cases (Fig. 4-6), the mitigating action begins at day 180. This is a strategy intended for an existing injection region; I wanted to initialize the model with pressure perturbations. The count of earthquakes

generated in each scenario is directly proportional to cumulative injected volume. For these cases, comparing injected volume and earthquake generation (Fig. 4-5) gives almost a perfect linear relationship (R^2 = 0.998). If I add the control case to the analysis, a linear approximation fits just as well (R^2 = 0.998). As would be expected, due to differences in total injected volume, the cycled reductions do not perform as well as the perpetual reduction in reducing the number of earthquakes occurring.
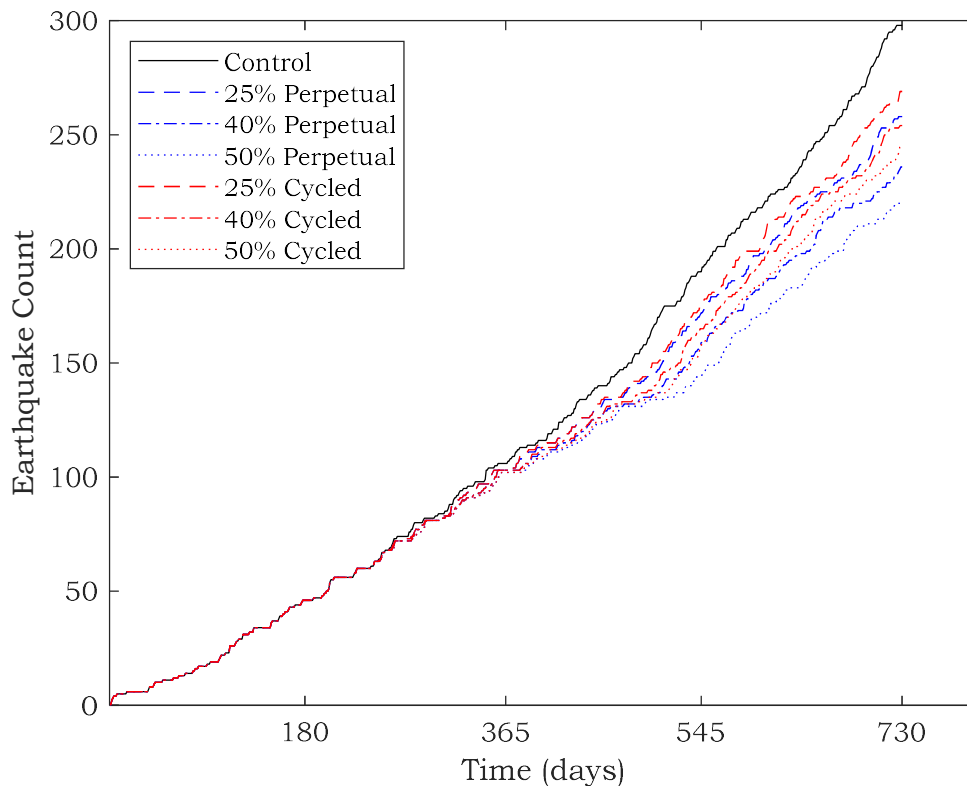
Figure 4-6 Earthquake count vs. time, injection reduction

For the TLS cases (Fig. 4-7), the mitigating action begins at day 180. Fig. 4-7 uses shared colors for TLS with the same magnitude thresholds. The traffic

lights see a wide range of effectiveness in reducing earthquake counts. The more aggressive traffic light mitigations, with stricter thresholds or longer (or infinite) reaction lengths greatly reduce the total count of earthquakes but also greatly decrease the total injected volume. The less strict cases reduce both earthquake count and injection level to a lesser extent. Again, we see a linear relationship between injected volume and earthquake count (Fig. 4-5), but with a slightly weaker trend (R^2 = 0.9091).
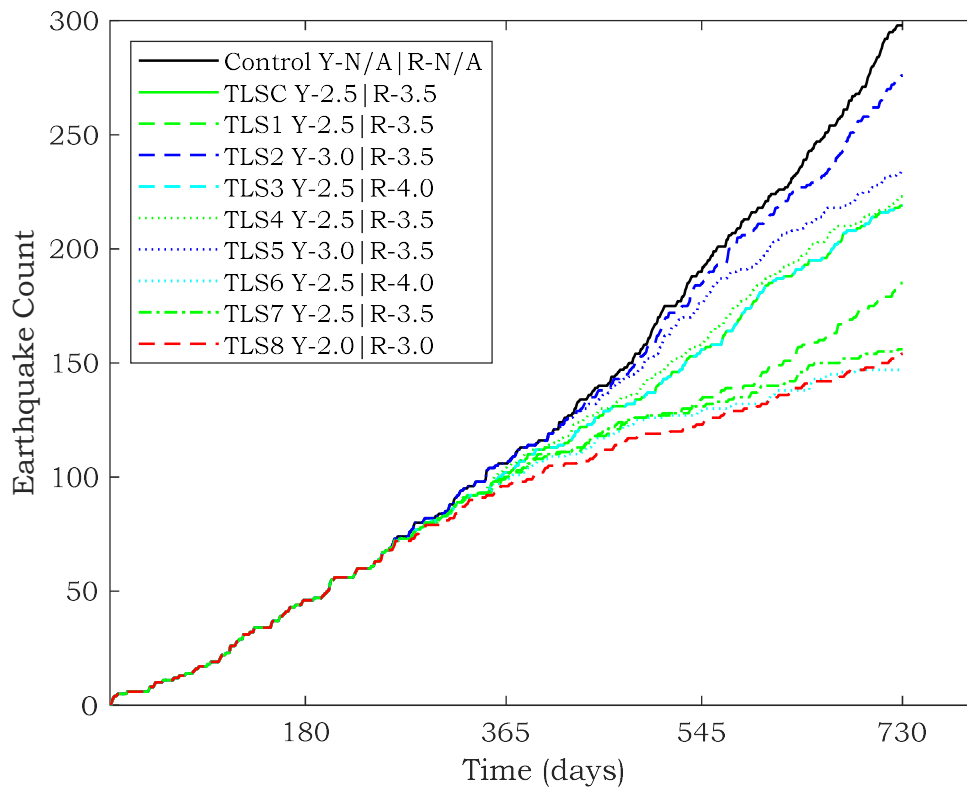
Figure 4-7 Earthquake count vs. time, traffic light systems. The legend indicates which Traffic Light scenario and the magnitudes triggering a yellow or red light.

Fig. 4-8 compares the four traffic light cases with a yellow-light threshold of $M_w2.5$ and a red-light threshold of $M_w3.5$. The red-light action in all four cases is to stop injection, while the yellow-light action in two cases is to reduce injection to 50% and in the other two cases to 75% of the control volume. The durations for yellow- and red-light actions also change. The 50% vs 75% reduction does not have a significant effect on reducing earthquake count but increasing the duration of mitigating action is very effective. Having a longer yellow-light duration keeps injection reduced for a greater time and allows a greater likelihood of a second yellow-light event that would mandate a red-light.
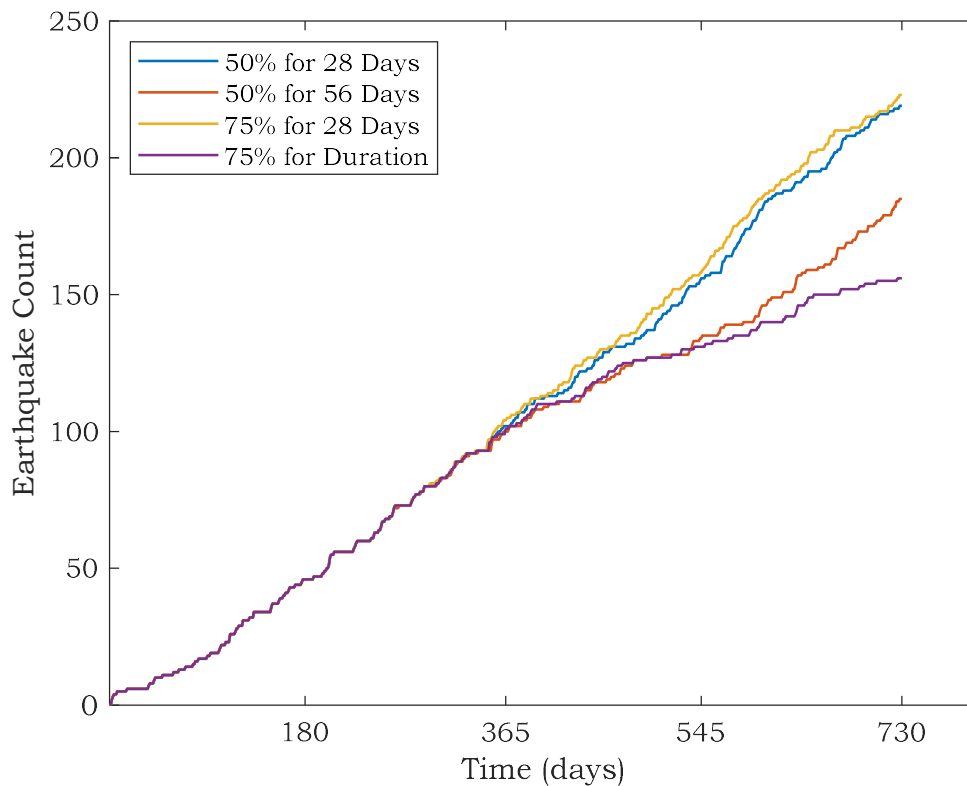
Figure 4-8 Earthquake count vs time, effect of reaction duration, yellow-light threshold of $M_w2.5$ and red-light threshold of $M_w3.5$

Fig 4-9 compares the effect of changing reaction magnitude thresholds. In my simulation, I do not see any change by changing the threshold for a red-light reaction. Increasing or decreasing the yellow-light threshold leads to a large change in the number of earthquakes induced by the operation. Likely my condition of two yellow-light events leading to a red-light condition controls over the red-light threshold.
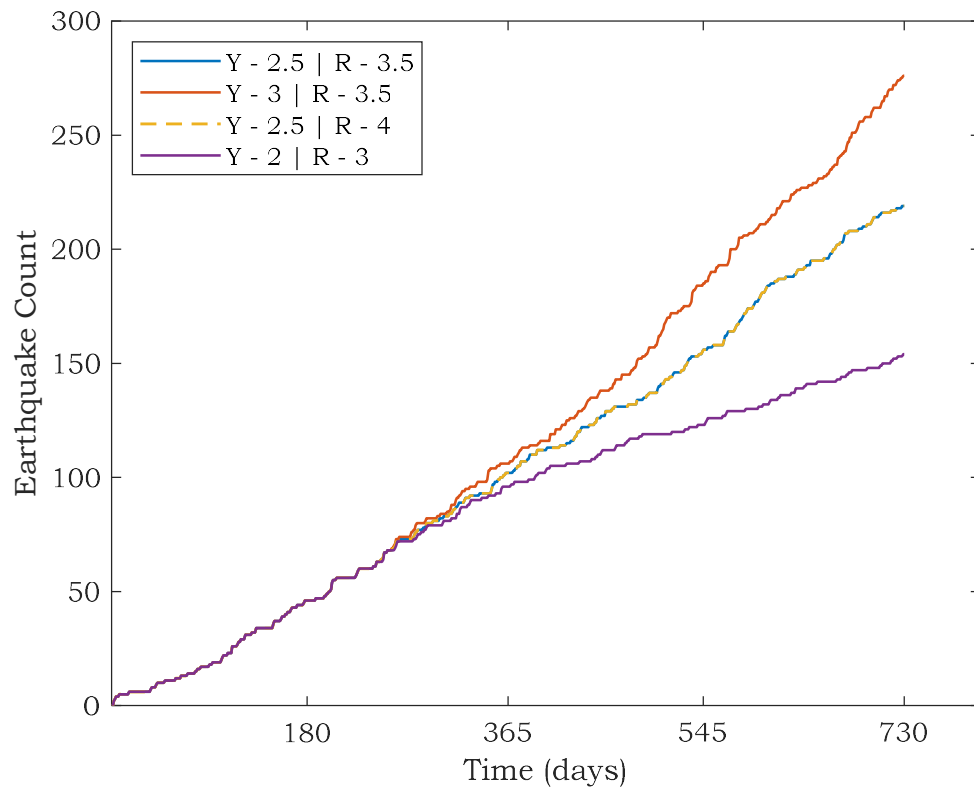
Figure 4-9 Earthquake count vs time, effect of thresholds for yellow and red lights

4.2 Ground Shaking Intensity

With the hydromechanical model's earthquake catalogs, I produce 100 new sets of magnitude realizations, leading to 100 unique earthquake catalogs for all the scenarios except for the TLS. I cannot do this step for the traffic light cases, as they are magnitude dependent and a new catalog would lead to yellow and red lights conditions at different times than the modeled case, changing the pressures that develop in the model.

I determine the ground motion intensity by calculating the median intensity for a given earthquake event (defined by magnitude and location) with the previously described ground motion model. An example ground motion intensity map with for a single set of intensity realizations for a $M_w4.4$ earthquake is shown in Fig. 4-10.
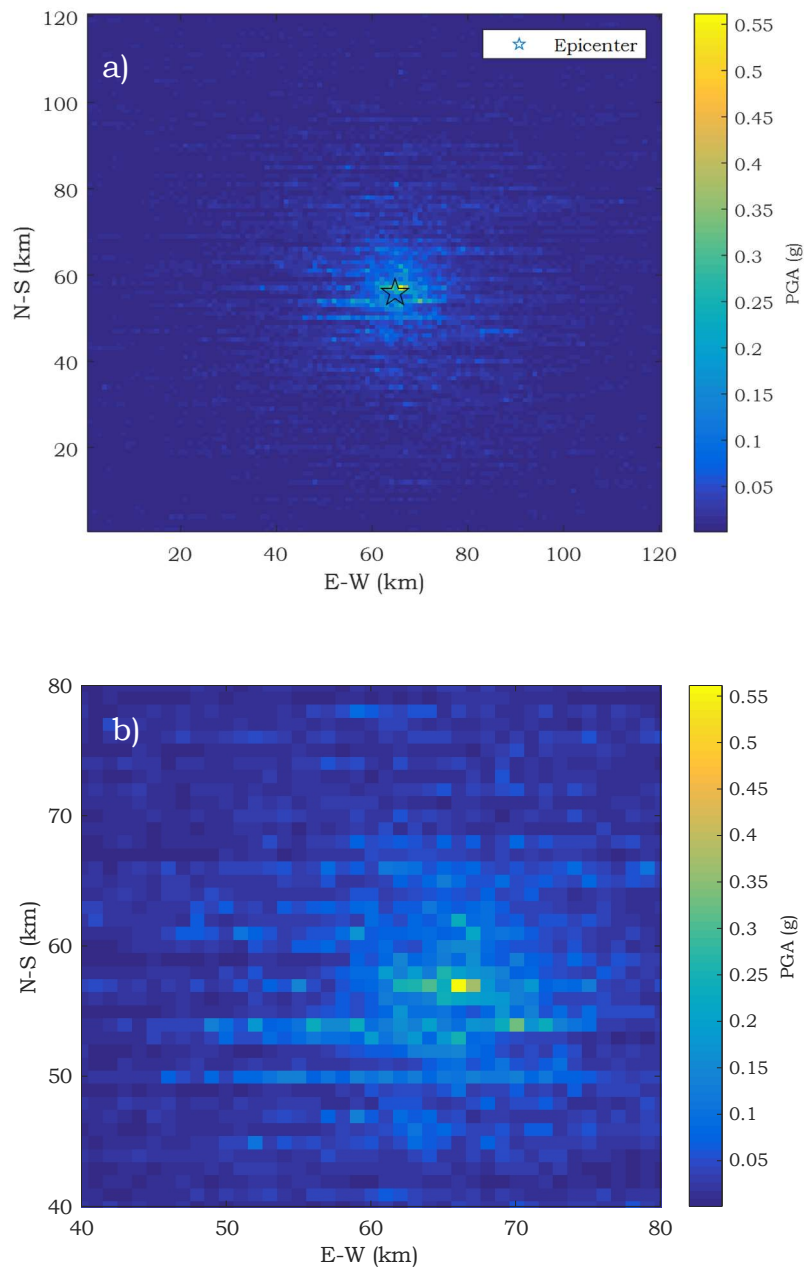
Figure 4-10 Peak ground acceleration for $M_w4.4$ earthquake, one realization

a) Extents of analysis region, b) Center 40 km by 40 km

In order to find the probability of ground motion intensity exceeding a threshold intensity, I compare all my ground motion maps to a threshold

intensity. I consider PGA thresholds of 0.1 g and 0.2 g. The first threshold is a

round number, and the second is the threshold where damage is expected

(Bommer, 2020). For each scenario, I have 100 earthquake catalogs with 100

ground motion intensity realizations for each earthquake. I determine the

frequency of every location exceeding the ground motion intensity thresholds

and divide that by the total number of realizations to determine the probability

of any location exceeding the thresholds. I can look at the area of each case

that exceeds threshold probabilities to see the extents of the region exceeding a

ground motion intensity.

Table 4-2 Area with greater than 10% probability of exceedance of PGA
thresholds

Scenario	Area (km²) exceeding 10% probability of	
	PGA ≥ 0.1g	PGA ≥ 0.2g
Control	276	29
S1	315	0
S2	304	1
S3	300	0
R1	272	35
R2	270	29
R3	270	34
R4	273	32
R5	275	32
R6	269	27

Table 4-2 shows that the increased spacing strategy does submit a larger

area subject to a greater than 10% probability of exceeding the specified

ground motion intensity threshold because a larger area sees a change in pore

pressure. When considering a greater ground motion intensity threshold, these

strategies begin to influence the reduction of ground motion hazard. A larger area is subject to earthquakes so some locations will have an elevated hazard. Overall, however, less earthquakes are generated and, therefore, the region is less likely to experience larger earthquakes.

There appear to be a few anomalies in these results. For instance, a few of the reduction cases appear to increase the probability of exceeding 0.2 g. This is a factor of the random generation involved in this procedure. The reduction cases do not appear to influence the area of the region where 0.2 g is likely.

Fig. 4-11 shows the probability of exceeding a PGA of 0.1g for the control case (Control; Fig. 4-11a), the 5 km increased spacing case (S3; Fig 4-11b), and the 40% injection reduction case (R2; 4-11c). Comparing the control (Fig. 4-10a) and the increased spacing (Fig. 4-11b), in the case with greater distance between wells, we see a wider area with some probability of exceedance, but a much smaller area of great probability. When considering ground motion intensities, the increased spacing cases add a small degree of hazard on a local scale as the wells are located further from the center while reducing hazard on a regional scale. Comparing the control (Fig. 4-11a) and the 40% reduction (Fig. 4-11c), the region with increased probability is roughly the same size and shape. The reduction cases appear to be ineffective when considering ground motion intensity reduction. The mitigation strategies still lead to a large number of earthquakes and, when the wells are tightly spaced, the

earthquakes are likely to happen in a more condensed area, giving the center great probability of shaking. All the earthquakes occur within the spatial extents of the control case, so the likelihood of ground motion intensity occurrence is spread over a smaller region than the increased spacing cases.
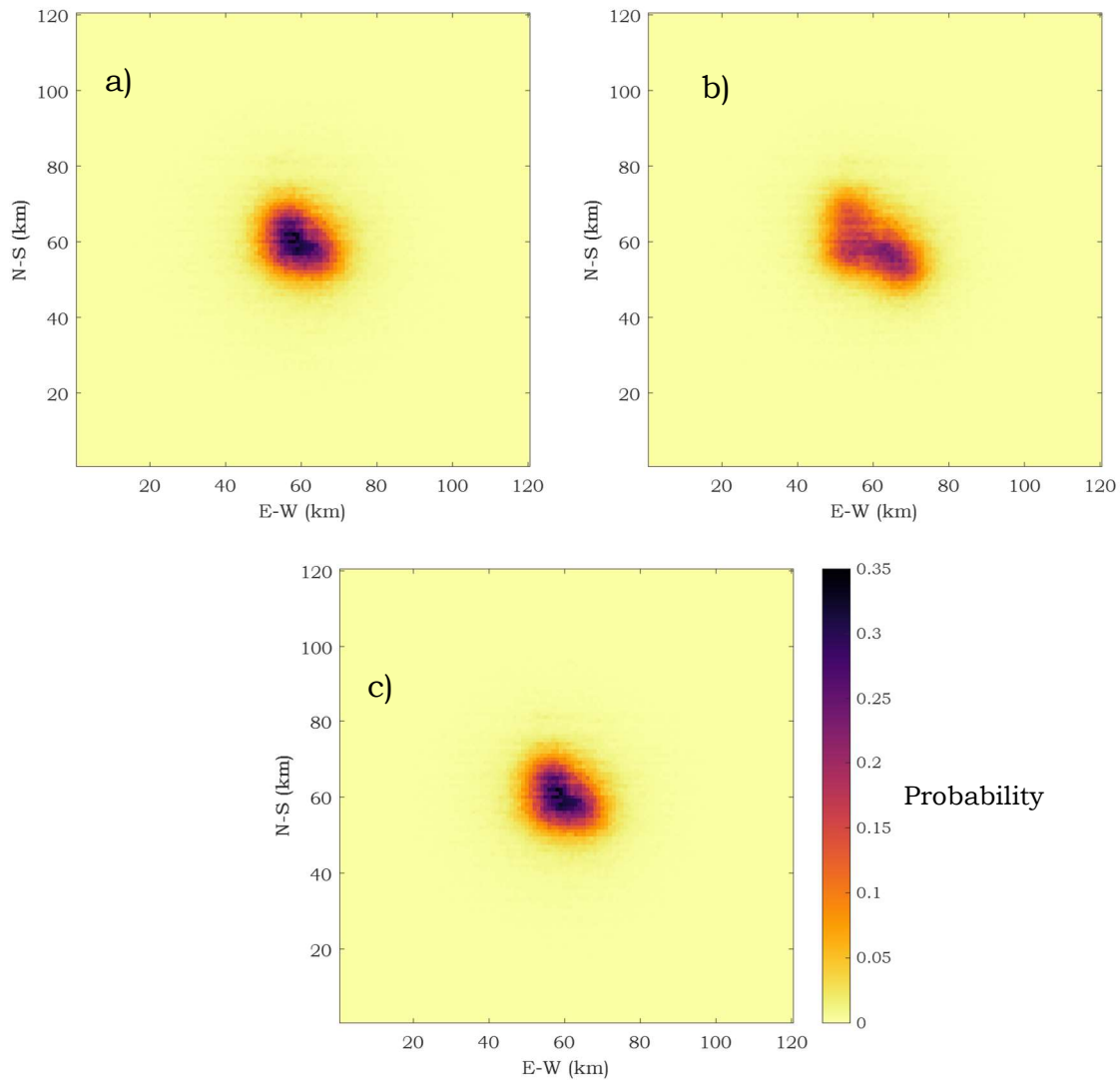
Figure 4-11 Probability of PGA at each location exceeding 0.1 g
a) control scenario, b) 5 km well spacing, and c) 40% reduction beginning at 180 days

4.3 Economic Losses

Loss is considered two ways. Chase et al. (2019) determined that repair costs do not tend to accumulate during a sequence of induced earthquakes; instead, repair costs are driven by the most damaging event in the series. Therefore, one of the values I am interested in is the highest repair cost from any earthquake in the two-year period. However, homeowners may choose to repair their home after any or every earthquake. Considering this, I am also interested in the sum of repair costs from all the earthquakes in the sequence.

4.3.1 Losses to Individual Building

I determine the loss in terms of repair cost by comparing the spectral acceleration at the fundamental period of my buildings to loss predictions I produced with SP3 for each of the structure types of interest. An example loss map for a single-family dwelling in an earthquake in the control scenario is shown in Fig. 4-12.
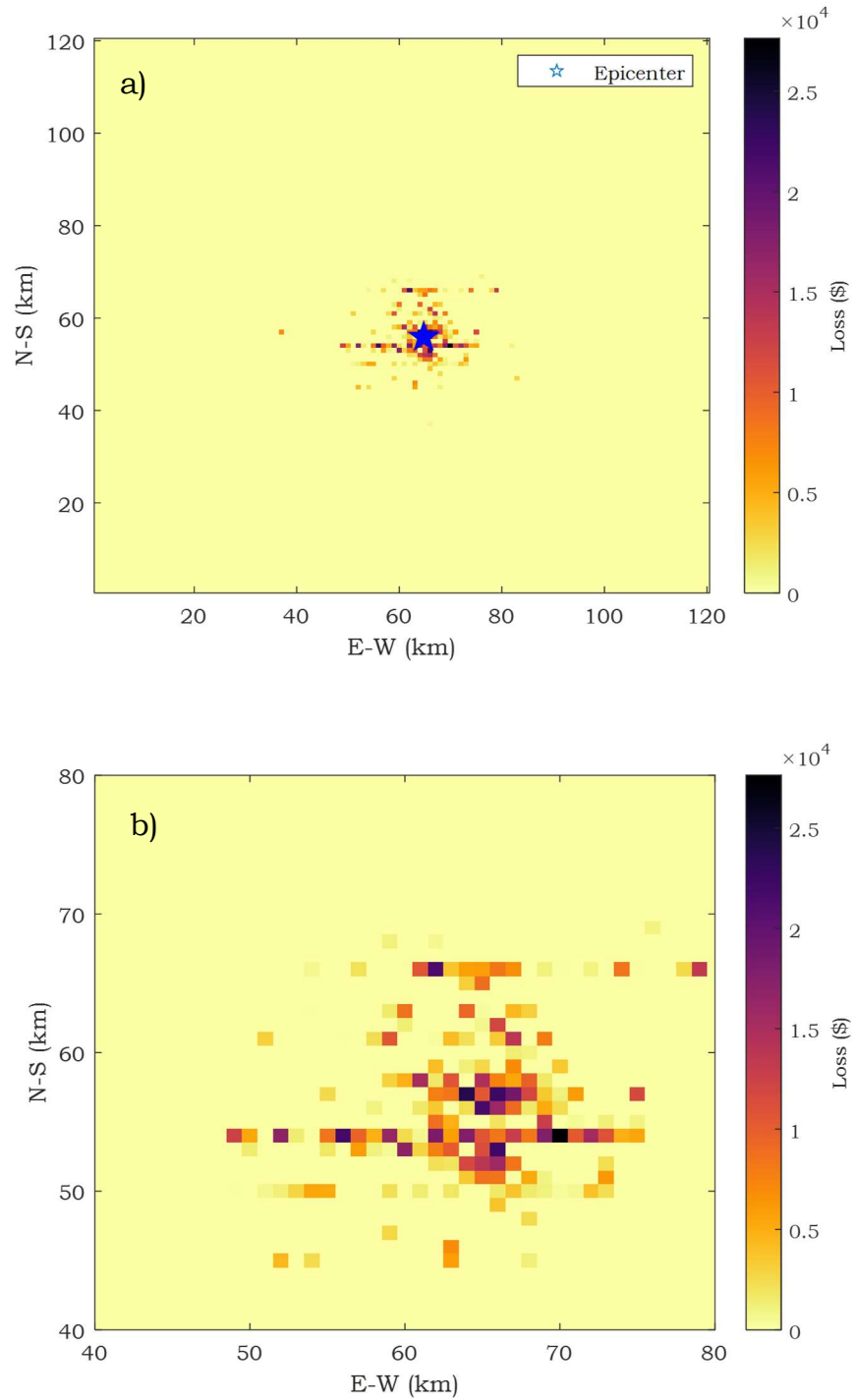
Figure 4-12 Single-family dwelling loss for $M_w4.4$ earthquake (same event as Fig. 4-10), one realization

a) Extents of analysis region, b) Center 40 km by 40 km

I am interested in how each mitigation scenario affects the risk to a single structure at any location in the region. I consider a loss threshold of 1% of building value for both a single- and multi-family dwelling; this value is selected because it is low enough that it can be expected some buildings will experience it from induced earthquakes, but high enough to be a significant burden on homeowners or insurance companies. For each scenario, I have 100 earthquake catalogs with 100 loss realizations for each earthquake for every 1 km by 1 km grid cell. I determine the frequency of every location exceeding the loss threshold and divide that by the total number of realizations to determine the probability of any location exceeding the thresholds. I can look at the area of each case that exceeds threshold probabilities to see the extents of the region exceeding a loss value. Fig. 4-13 shows, for the control case, the probability of exceeding 1% of SFD value in assuming repairs after every event.
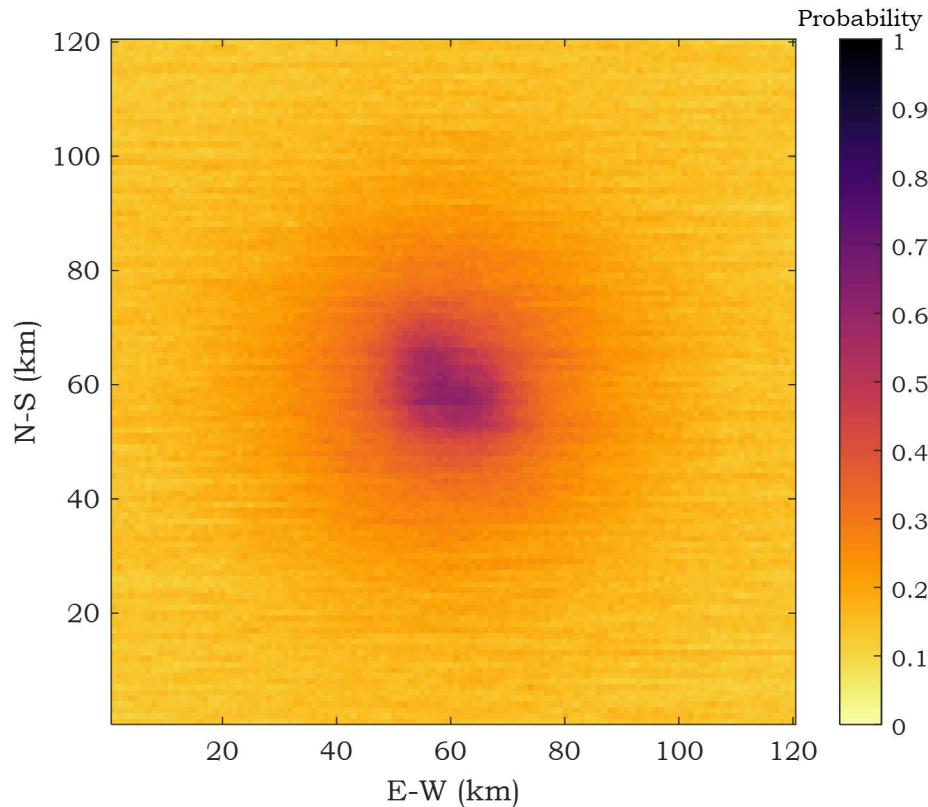
Figure 4-13 Probability of exceeding 1% loss for the SFD, repairing after each event, control case

Table 4-3 shows the area where the probability of loss, given repair costs driven by the most damaging event, exceeds certain thresholds for a MFD. Table 4-4 shows the area of which the probability of loss given repair after each event exceeds the same thresholds for a MFD. Corresponding tables for the SFD can be found in the appendix, Tables A-1 and A-2. Fig. 4-14 shows that for both single- or multi-family structures, the area where the probability of damage exceeds the 1% threshold is orders of magnitude greater when considering multiple repairs because most of the damaging earthquake events

lead to non-structural, cosmetic damage. The weakest or most damageable

components, once repaired, are likely to be damaged again in a subsequent

earthquake.

Table 4-3 Area with probability of MFD loss, given one repair, exceeding 1% of building value

Scenario	Area (km²) with probability of loss in any motion exceeding 1% of building value	
	P(Exceed) > 10%	P(Exceed) > 50%
Control	287	0
S1	303	0
Peak	281	0
S3	270	0
R1	278	0
R2	275	0
R3	270	0
R4	275	0
R5	280	0
R6	272	0

Table 4-4 Area with probability of MFD loss, given repair after every damaging event, exceeding 1% of building value

Scenario	Area (km²) with probability of total loss exceeding 1% of building value	
	P(Exceed) > 10%	P(Exceed) > 50%
Control	14333	263
S1	13110	179
S2	13400	189
S3	10409	85
R1	13231	203
R2	11050	170
R3	9260	145
R4	13784	218
R5	13101	197
R6	12036	176
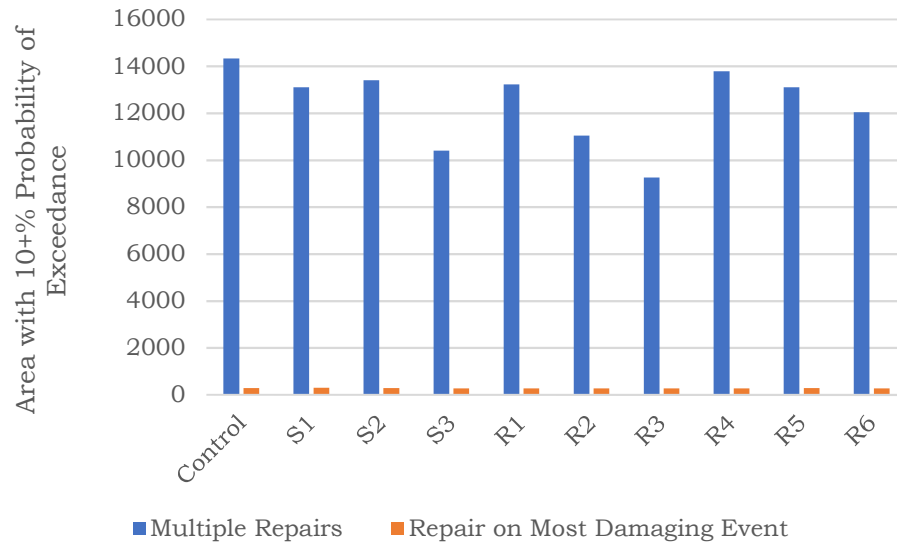
Figure 4-14 Area with greater than 10% probability of exceeding 1% of building value, MFD

Fig. 4-15 shows that SFD and MFD follow similar trends across the different mitigation strategies. In every scenario, the MFD has a smaller region where loss is expected to exceed 1% of building value. This could be due to the MFD having replacement cost over three times greater and, therefore, it takes more damage to reach the 1% threshold.
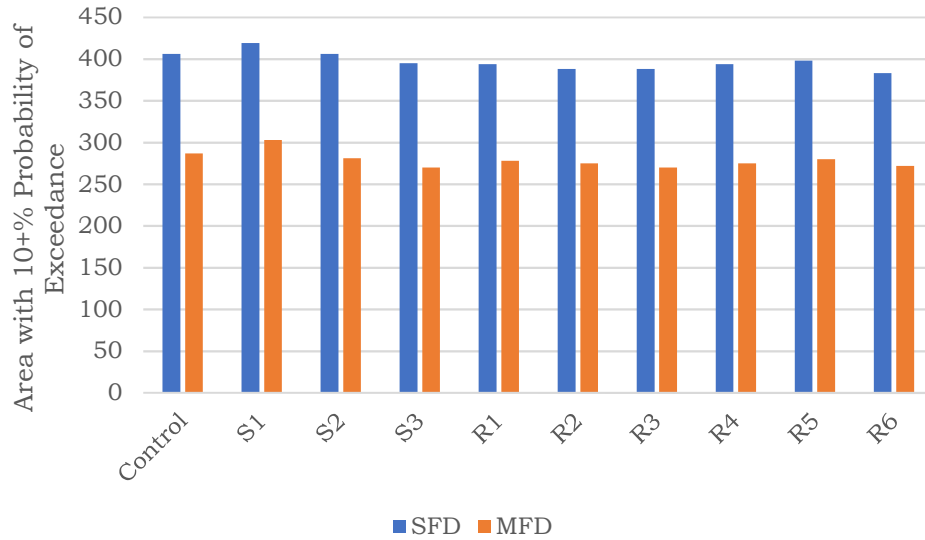
Figure 4-15 Area with greater 10% probability of exceeding 1% of building value, one repair

These loss values follow a similar pattern to the ground motion probabilities for the alternative spacing cases. Greater well spacing leads to an unchanged or greater area of the region with a low probability of exceeding 1% of building value, but a much smaller area with higher probabilities of exceedance. Increasing well spacing by 2 kilometers reduces the area with a 50% probability of exceeding the 1% damage threshold to 14.9% and 32.3% of area found in the control scenario for SFD and MFD, respectively, assuming repair after every damaging event.

Unlike ground motion intensity, reducing injection is effective at reducing the likelihood of loss. Ground motion intensity probability is related to only the strongest event while loss probability, assuming repair after each damaging event, is related to the number of damaging events. As the total number of earthquakes decrease, I expect fewer damaging earthquakes.

4.3.2 Losses to Building Inventory

The goal of mitigation is to lower earthquake risk to communities. I run my loss model with my three town archetypes to get better insight to how risk to groups of structures is affected. As for loss to a single structure, I realize loss for each structure in my inventory once for each ground motion intensity and sum over the entire inventory at each realization. The median repair cost values for the large town inventory at each location (Table 3-2) for a single repair and multiple repairs are shown in Tables 4-5 and 4-6 below.

Table 4-5 Repair cost to large town, given one repair on the most damaging event

Scenario	Loss from most damaging event		
	Large - Near	Large - Middle	Large - Far
Control	$15,300,000	$413,000	$173,000
S1	$6,240,000	$339,000	$149,000
S2	$5,720,000	$369,000	$153,000
S3	$5,290,000	$349,000	$138,000
R1	$12,100,000	$373,000	$155,000
R2	$9,710,000	$359,000	$141,000
R3	$9,560,000	$355,000	$136,000
R4	$14,300,000	$373,000	$161,000
R5	$12,600,000	$353,000	$149,000
R6	$12,400,000	$351,000	$143,000

Table 4-6 Repair cost to large town, given repairs after each event

Scenario	Total loss over two-year simulation		
	Large - Near	Large - Middle	Large - Far
Control	$29,200,000	$1,290,000	$544,000
S1	$9,870,000	$1,020,000	$439,000
S2	$13,300,000	$1,140,000	$469,000
S3	$8,660,000	$945,000	$377,000
R1	$21,100,000	$1,100,000	$452,000
R2	$16,700,000	$947,000	$383,000
R3	$15,100,000	$878,000	$357,000
R4	$24,200,000	$1,220,000	$494,000
R5	$21,900,000	$1,070,000	$445,000
R6	$22,700,000	$992,000	$415,000

Unsurprisingly, the locations closest to the injection region are most affected by the mitigating action. The strategies that are most successful at reducing loss to an individual town at close distances are the increased well spacing strategies. At an intermediate distance, the injection reduction cases begin to show better performance in decreasing risk. This is likely because the earthquakes are a little more dispersed in the increased spacing cases, increasing the risk at further distances from the injection region when compared to the reduction cases.

These loss values suggest an exclusion zone could also be very effective. When compared to a town located in the center of the injection region in the control scenario, a large town 20 km (about 12 miles) away from the edge of an injection region sees only 2.7% of the damage from the most damaging event or 4.4% of the damage from all events over the two-year analysis period.

I consider a similar analysis for the archetype region I've created (Fig. 3-15). The loss values in the Fig. 4-16 below are median repair costs for the entire inventory of the archetypal region. These values can be found in the appendix, Table A-3. Here, we see some of reduction cases performing better, relative to their effect on intensity, in decreasing loss to the inventory, especially when considering the most damaging event (particularly R3). When considering the sum of all losses, increased well spacing begins to be more effective. The cycled reductions perform similarly to the perpetual reductions when considering repair costs after each event. When considering the most damaging event, however, the perpetual reductions perform significantly better. The likelihood of a large event increases as total number of earthquakes increase, so having additional earthquakes in the catalog is expected to lead to a stronger controlling earthquake.
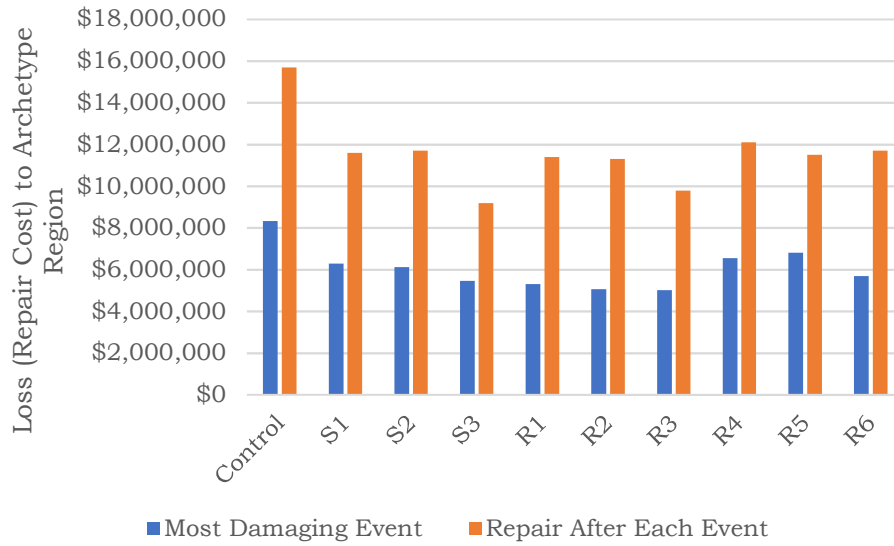
Figure 4-16 Loss to archetype region

4.3.3 Mitigation Performance Number

In this section, I propose a quantity I call the mitigation performance number (MPN) to evaluate how effective each strategy is at reducing loss, while also limiting interruption to injection operations when compared to the control scenario. For this value, I am defining loss as repair costs assuming repair after every event. The MPN is defined by Equation 1, where w_1 and w_2 are user defined weights:

$$MPN = \frac{w_1*(\% \, Injected)+w_2*(\% \, Decrease \, in \, Total \, Loss)}{w_1+w_2} \quad (1)$$

Where:

$$\% \, Injected = \frac{Injected \, Volume \, in \, Mitigating \, Scenario}{Injected \, Volume \, in \, Control \, Scenario} \quad (2)$$

And

$$\% \ Decrease \ in \ Total \ Loss \ = \ 1 - \frac{Loss \ Assuming \ Repair \ After \ Every \ Event \ in \ Mitigating \ Scenario}{Loss \ Assuming \ Repair \ After \ Every \ Event \ in \ Control \ Scenario} \quad (3)$$

For the purpose of this thesis, I consider equal weights ($w_1 = 1.0$ and $w_2 = 1.0$) and I consider change in loss being twice as important ($w_1 = 1.0$ and $w_2 = 2.0$). Given stakeholder input, these weights could be refined for a particular injection operation. MPN is directly proportional to percent of control scenario injection and the percent decrease in total repair cost to the region. Therefore, greater MPNs are desirable.

The MPN for every mitigation scenario is given in Table 4-7. For the equal weight MPN, any value greater than the control scenario's MPN of 0.5 is effective. For the case when loss is twice as important, any value greater than the control scenario's MPN of 0.33 is effective. The increased spacing cases were very effective at reducing the regional loss with no change in total injection operations and perform very well in terms of MPN. Case S3 will appear as most efficient, regardless of weighting, because it reduces the percentage of total loss by the greatest amount, without affecting injection volume to any extent. The reduction cases do not appear nearly as effective as the increased spacing cases with the weightings I have used. Scenario R2 (40% injection reduction), appears inefficient when both quantities are given equal weighting. While the reduction cases all reduce regional loss, they greatly decrease the volume of injected wastewater. When loss is given a greater

importance with greater w_2, we begin to see reduction scenario MPNs of greater

magnitude, meaning they are regarded as more effective.

Table 4-7 Mitigation Performance Number

			MPN	
Scenario	% Injected	Change in % Loss	$w_1=1$ $w_2=1$	$w_1=1$ $w_2=2$
Control	1.00	0.00	0.50	0.33
S1	1.00	0.26	0.63	0.51
S2	1.00	0.25	0.63	0.50
S3	1.00	0.41	0.71	0.61
R1	0.81	0.27	0.54	0.45
R2	0.70	0.28	0.49	0.42
R3	0.63	0.38	0.50	0.46
R4	0.88	0.23	0.55	0.44
R5	0.80	0.27	0.53	0.45
R6	0.75	0.25	0.50	0.42

A conclusion I can draw from this is that injection reduction is not as

strong of a linear relationship to improved loss performance (R^2 = .747). Lower

levels of reduction are more efficient at reducing inventory loss, while leading to

the least interruption in injection. On average, the cycled reduction cases

perform about as well as the perpetual reduction. For the perpetual reduction,

the percentage of total loss does not appear to greatly change by further

reducing injection. They all see roughly the same change in loss even as

injection is further cut. Therefore, the case that reduces the injection the least

(R4) appears to be the best performing when weights are equal even though

lower losses are seen in the greater reduction cases. Fig. 4-17 compares the

reduction cases in their effect of reducing loss with respect to injected volume.
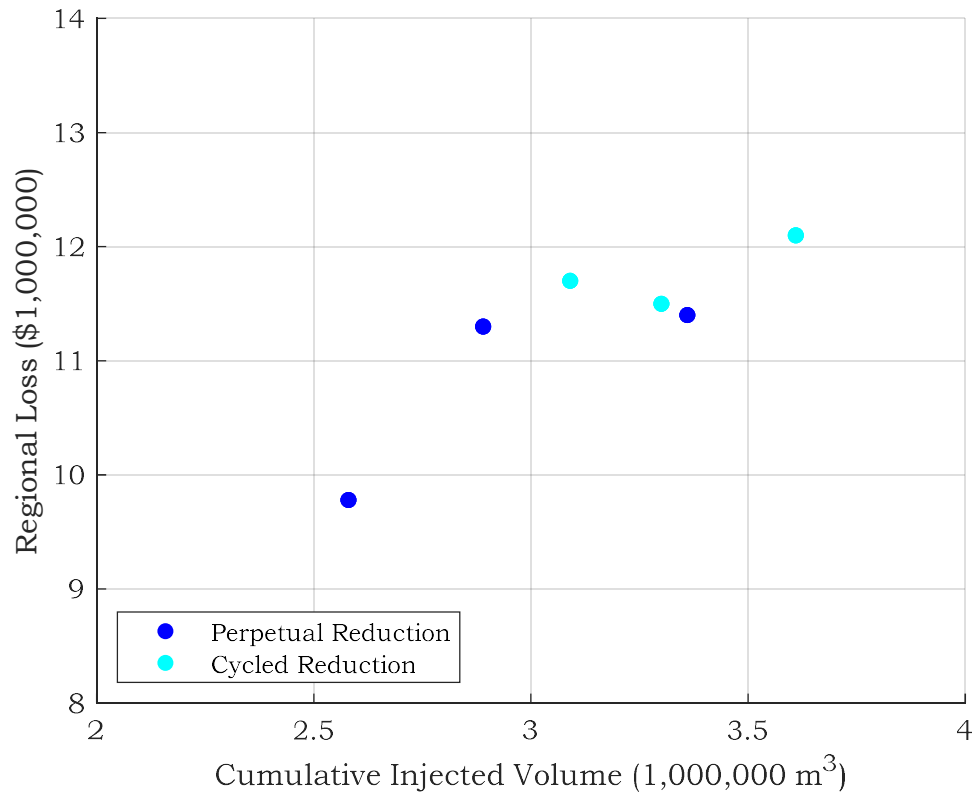
Figure 4-17 Cumulative injected volume vs. regional loss, reduction scenarios

A graphical representation of the MPN, considering equal weight, is given in Fig. 4-18. A graphical representation of the MPN, considering loss reduction with a weight of 2.0, is given in Fig. 4-19. The relations of the MPNs of R1-R3 and R4-R6 change with the weighting adjustment because the change in loss is not directly proportional to the change in injection.
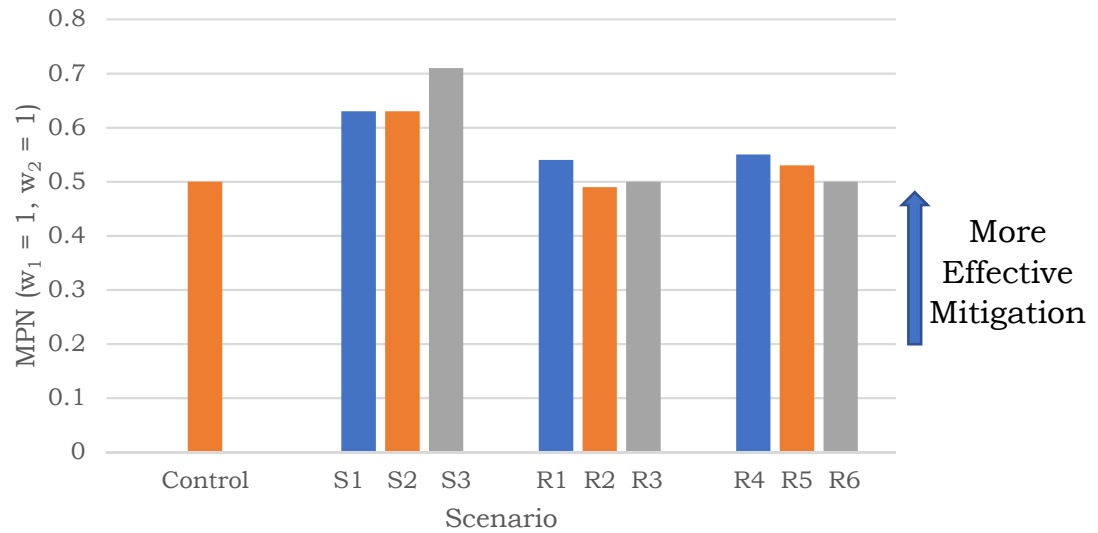
Figure 4-18 Mitigation performance number, equal weighting of losses and injection
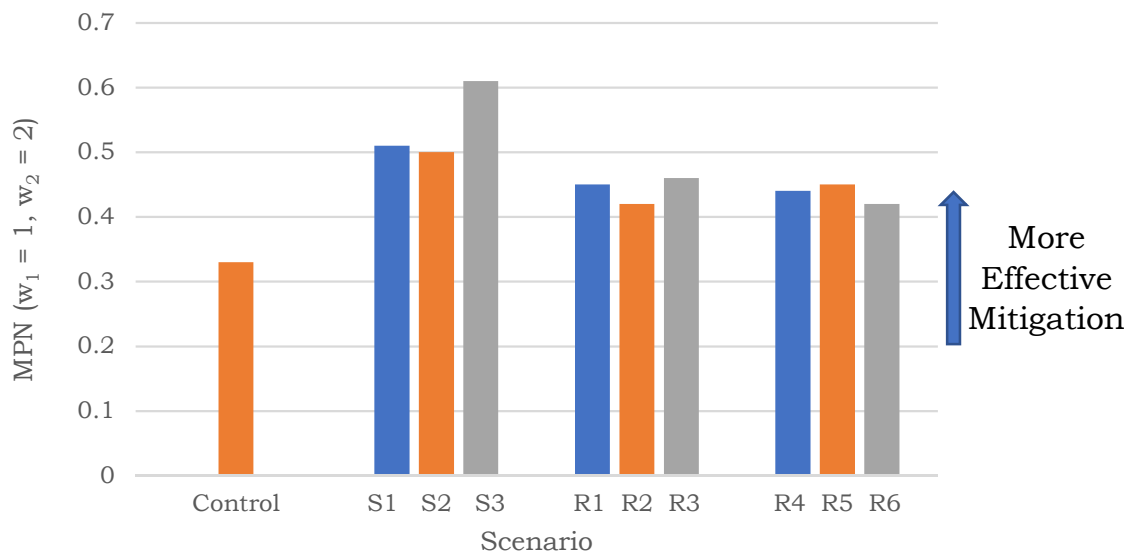
Figure 4-19 Mitigation performance number, loss weighted twice as much as injected volume

Fig. 4-20 is an alternative visualization of the MPN in Fig. 4-19, with a gradient to better depict how the two inputs interact. The cases along the top

row are the control and the increased spacing scenarios, where injected volume does not change. Changing the weighting of the two input parameters changes the slope of the contour lines but not the location of the data points. If the contours change, the MPN for that point is also changed.
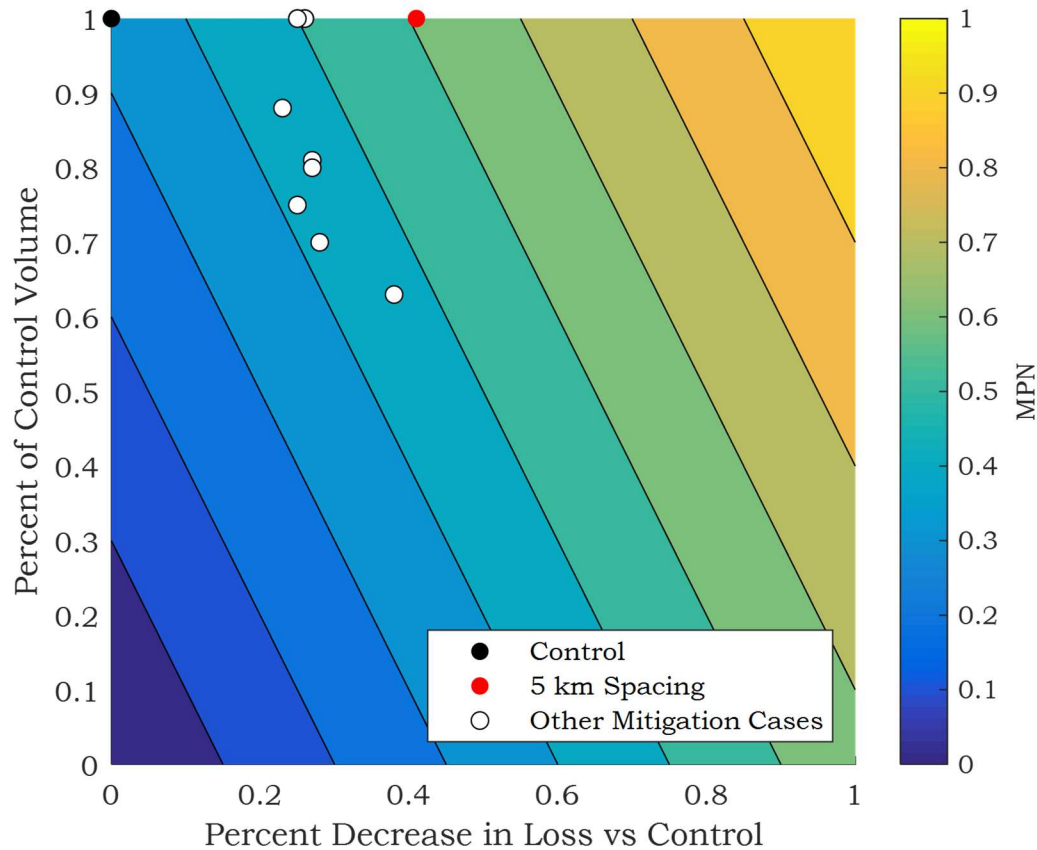
Figure 4-20 MPN gradient plot, loss weighted twice as much as injected volume

5 Conclusion

This study compares three strategies for mitigation seismic risks associated with deep wastewater injection. I consider increasing the spacing between injection wells, overall reduction in injection rates, and reactive traffic light systems. I use a hydromechanical model to simulate two years of injection for each scenario. I analyze the outputted earthquake catalog in ground motion and loss models to determine how each strategy affects risk, in terms of economic loss, to residential structures.

I find all three strategies are effective to some degree at reducing expected loss to a region from wastewater-injection induced earthquakes. However, each strategy also has some drawbacks. I compare key metrics of the spacing and reduction cases in Fig. 5-1.
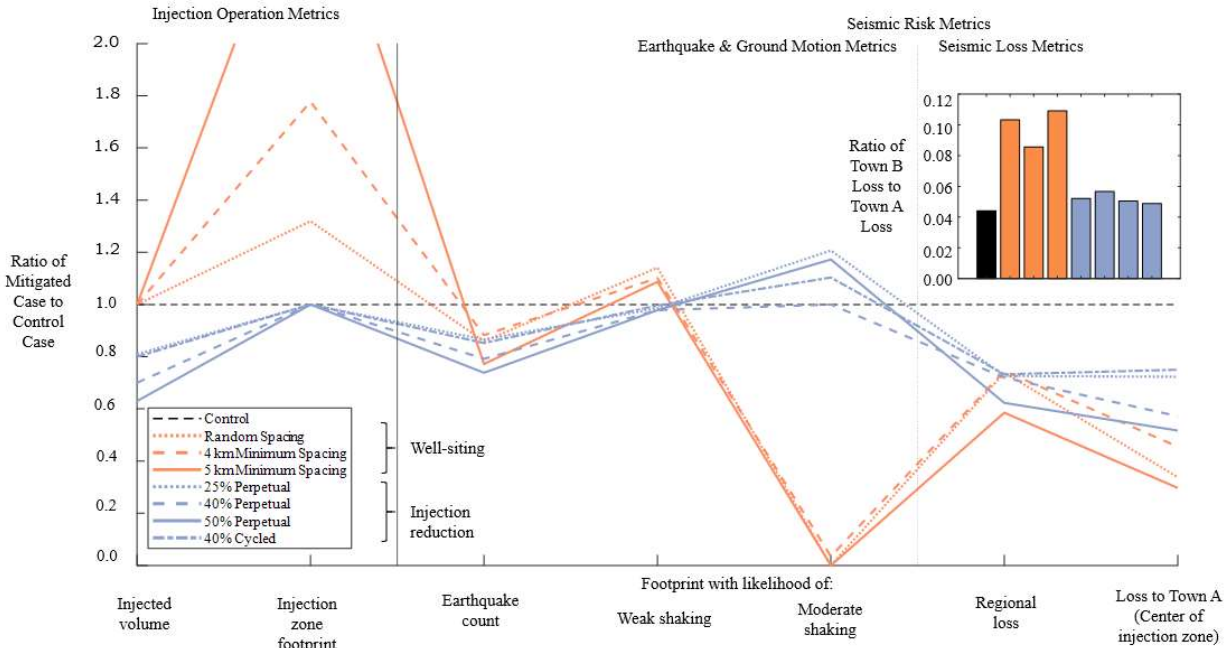
Figure 5-1 Comparison of key metrics for spacing and reduction cases

"Injection zone footprint" is defined only by the locations of the injection wells. "Likelihood of weak (or moderate) shaking" is defined by 10% probability of exceeding 0.1 g and 0.2 g respectively. For the inset chart, "Town B" is the town located 20 km from the injection zone boundary.

The increased well spacing cases are all found to greatly reduce risk on the archetype region, by 26 - 41% of total repair costs. However, on a more local scale, because the wells have a greater footprint than in the control case, a greater area is subject to some degree of hazard. Considering the overall reduction in loss, this is a promising strategy for new injection wells.

The injection reduction cases and traffic light cases both reduce the number of earthquakes generated in the simulation. When comparing earthquake generation to total injected volume of wastewater, the injection reduction is more efficient at reducing earthquake counts than the traffic light

systems. On a per volume basis, the overall reduction cases lead to fewer earthquakes. The injection reduction cases are found to reduce the expected loss to the archetype region by 23 – 38%. Injection reduction leads to a linear decrease in earthquake generation, but regional loss does not appear to have great differences in the reduction scenarios I consider. This is due to earthquake magnitudes having a nonlinear distribution. Reducing the number of small earthquakes by a great extent does not reduce the number of large earthquakes by the same extent.

Traffic lights are found to vary greatly in effectiveness in reducing risk. The TLS that have lower thresholds, greater prescribed reductions, and longer durations all reduce loss significantly more than the less restrictive TLS. The primary disadvantage of both strategies is that they greatly reduce the total injected volume of wastewater.

To evaluate reduction in injection volumes relative to reduction in risk, I define a mitigation performance number or MPN. The increased well spacing strategy has the greatest MPN, meaning it is most effective at reducing regional loss compared to injected volume of wastewater because it does not reduce injection. I would suggest, particularly for a new injection operation, to allocate additional distance between injection wells and an exclusion zone from critical infrastructure and population centers. I find that my large town has greater than 95% reduction in loss by moving it from the middle of an injection region

to 20 km away from the edge of the region, even with no other mitigating action.

Further research could expand on a few parts of this study. Greater computing resources would allow me to better evaluate the TLS strategy. In this study, we ran the hydromechanical model once for each mitigation scenario and captured magnitude uncertainty by re-generating the earthquake magnitudes in that catalog. I cannot re-generate magnitudes in the magnitude-dependent TLS. With greater computing resources, I could run the hydromechanical model 100 times to create the same number of catalogs as used in the other strategies. I do not expect this would greatly affect my findings. I find that the overall reduction cases are more effective than TLS at reducing earthquake counts on a per-volume basis.

A hydromechanical model with fault stress-strain properties could predict "actual" magnitudes as opposed to the probability distribution of magnitudes I have assumed. For a generic region, the fault distribution would need to be regenerated many times to capture uncertainty in fault locations and orientations. Additionally, a fully-coupled true three-dimensional model (instead of the pseudo three-dimensional one I have used for this study), would allow one to investigate the effect of adjusting injection depth. This would also provide more accurate pressure perturbations when considering depth. This improved model would be considerably more computationally expensive than the pseudo three-dimensional one used here.

Additional structure types should be considered in loss analysis. The building stock of Oklahoma includes more than just two-story light frame wood residential buildings. Moreover, additional mitigation strategies should also be considered. A cost-benefit analysis on strengthening the regional building stock or population relocation could prove interesting.

Alternative types of induced seismicity could be considered if one uses a different model for generating earthquakes given an operation. This would allow a researcher to investigate mitigating actions for gas extraction, hydraulic fracturing, enhanced geothermal systems, or any other cause for human induced earthquakes.

Bibliography

Alnæs, M. S., Blechta, J., Hake, J., Johansson, A., Kehlet, B., Logg, A., Richardson, C., Ring, J.,

Rognes, M. E., & Wells, G. N. (2015). The FEniCS Project Version 1.5. *Archive of*

Numerical Software, *3*(100). https://doi.org/10.11588/ans.2015.100.20553

Assatourians, K., & Atkinson, G. M. (2020). Processed ground-motion records from induced

earthquakes for use in engineering applications. *Canadian Journal of Civil Engineering*,

47(1), 96–108.

ATC. (2019). *Active Projects: ATC-116-5*. ATC. atcouncil.org/atc-116-5

Atkinson, G. M. (2017). Strategies to prevent damage to critical infrastructure due to induced

seismicity. *FACETS*, *2*(1), 374–394. https://doi.org/10.1139/facets-2017-0013

Atkinson, G. M., Eaton, D. W., Ghofrani, H., Walker, D., Cheadle, B., Schultz, R., Shcherbakov,

R., Tiampo, K., Gu, J., Harrington, R. M., Liu, Y., Baan, M. van der, & Kao, H. (2016).

Hydraulic Fracturing and Seismicity in the Western Canada Sedimentary Basin.

Seismological Research Letters, *87*(3), 631–647. https://doi.org/10.1785/0220150263

Baird, B. W., Liel, A. B., & Chase, R. E. (2020). Magnitude Thresholds and Spatial Footprints of

Damage from Induced Earthquakes. *Earthquake Spectra*, *In Press*.

Baisch, S., Koch, C., & Muntendam-Bos, A. (2019). Traffic Light Systems: To What Extent Can

Induced Seismicity Be Controlled? *Seismological Research Letters*, *90*(3), 1145–1154.

https://doi.org/10.1785/0220180337

Baker, J., & Jayaram, N. (2008). Correlation of Spectral Acceleration Values from NGA Ground

Motion Models. *Earthquake Spectra - EARTHQ SPECTRA*, *24*.

https://doi.org/10.1193/1.2857544

Baker, T. (2015). *Media Advisory—Ongoing OCC Earthquake Response*. Oklahoma Corporation Commission. http://www.occeweb.com/News/2015/03-25-15%20Media%20Advisory%20-%20TL%20and%20related%20documents.pdf

Barba-Sevilla, M., Baird, B. W., Liel, A. B., & Tiampo, K. F. (2018). Hazard implications of the 2016 Mw 5.0 Cushing, OK earthquake from a joint analysis of damage and InSAR data. *Remote Sensing*, *10*(11), 1715.

Birdsell, D. T., Karra, S., & Rajaram, H. (2018, June). *Code development for modeling induced seismicity with flow and mechanics using a discrete fracture network and matrix formulation with evolving hydraulic diffusivity.* 52nd US Rock Mechanics / Geomechanics Symposium and 2nd Discrete Fracture Network Engineering Conference, Seattle, WA.

Bommer, J. J. (2020, March 5). *From Earthquakes Big to Small: How to Frame the Earthquake Hazard Conversation*. 2020 National Earthquake Conference, San Diego, CA.

Bommer, J. J., Crowley, H., & Pinho, R. (2015). A risk-mitigation approach to the management of induced seismicity. *Journal of Seismology*, *19*(2), 623–646. https://doi.org/10.1007/s10950-015-9478-z

Brown, M. R. M., Ge, S., Sheehan, A. F., & Nakai, J. S. (2017). Evaluating the effectiveness of induced seismicity mitigation: Numerical modeling of wastewater injection near Greeley, Colorado. *Journal of Geophysical Research: Solid Earth*, *122*(8), 6569–6582. https://doi.org/10.1002/2017JB014456

Carslaw, H. S., & Jaeger, J. C. (1959). Conduction of heat in solids. *Oxford: Clarendon Press, 1959, 2nd Ed.*

Catalli, F., Rinaldi, A. P., Gischig, V., Nespoli, M., & Wiemer, S. (2016). The importance of earthquake interactions for injection-induced seismicity: Retrospective modeling of the Basel Enhanced Geothermal System. *Geophysical Research Letters*, *43*(10), 4992–4999. https://doi.org/10.1002/2016GL068932

Chase, R. E., Liel, A. B., Luco, N., & Baird, B. W. (2019). Seismic loss and damage in light-frame wood buildings from sequences of induced earthquakes. *Earthquake Engineering & Structural Dynamics*, *48*, 1365–1383.

Cornell, C. A. (1968). Engineering seismic risk analysis. *Bulletin of the Seismological Society of America*, *58*(5), 1583–1606.

Crain, K. D., & Chang, J. C. (2018). *Elevation Map of the Top of the Crystalline Basement in Oklahoma and Surrounding States*. 6.

Dempsey, D., & Riffault, J. (2019). Response of Induced Seismicity to Injection Rate Reduction: Models of Delay, Decay, Quiescence, Recovery, and Oklahoma. *Water Resources Research*, *55*(1), 656–681. https://doi.org/10.1029/2018WR023587

Dempsey, D., Suckale, J., & Huang, Y. (2016). Collective properties of injection-induced earthquake sequences: 2. Spatiotemporal evolution and magnitude frequency distributions. *Journal of Geophysical Research: Solid Earth*, *121*(5), 3638–3665. https://doi.org/10.1002/2015JB012551

Downey, P. (2017). *UIC INJECTION VOLUMES 2014*. Oklahoma Corporation Commision. www.occeweb.com/og/2014 1012A UIC volumes.xlsx

FEMA. (2018). *Seismic Performance Assessment of Buildings* (P-58-1).

Frohlich, C., DeShon, H., Stump, B., Hayward, C., Hornbach, M., & Walter, J. I. (2016). A Historical Review of Induced Earthquakes in Texas. *Seismological Research Letters*, *87*(4), 1022–1038. https://doi.org/10.1785/0220160016

Gischig, V. S., & Wiemer, S. (2013). A stochastic model for induced seismicity based on non-linear pressure diffusion and irreversible permeability enhancement. *Geophysical Journal International*, *194*(2), 1229–1249. https://doi.org/10.1093/gji/ggt164

Goebel, T. H. W., Weingarten, M., Chen, X., Haffener, J., & Brodsky, E. E. (2017). The 2016 Mw5.1 Fairview, Oklahoma earthquakes: Evidence for long-range poroelastic triggering at >40 km from fluid disposal wells. *Earth and Planetary Science Letters*, *472*, 50–61. https://doi.org/10.1016/j.epsl.2017.05.011

Gupta, A., & Baker, J. W. (2019). A framework for time-varying induced seismicity risk assessment, with application in Oklahoma. *Bulletin of Earthquake Engineering*, *17*(8), 4475–4493. https://doi.org/10.1007/s10518-019-00620-5

Gutenberg, B., & Richter, C. F. (1954). *Seismicity of earth and associated phenomenon* (2nd ed.). Princeton University.

Harvey, P. S., Heinrich, S. K., & Muraleetharan, K. K. (2017). A Framework for Post-Earthquake Response Planning in Emerging Seismic Regions: An Oklahoma Case Study. *Earthquake Spectra*, *34*(2), 503–525. https://doi.org/10.1193/053117EQS100M

Haselton, C., & Baker, J. (n.d.). *The FEMA P-58 Methodology and the Seismic Performance Prediction Program (SP3)*. Retrieved February 11, 2020, from hbrisk.com/sp3

Healy, J. H., Rubey, W. W., Griggs, D. T., & Raleigh, C. B. (1968). The denver earthquakes. *Science*, *161*(3848), 1301–1310.

Hincks, T., Aspinall, W., Cooke, R., & Gernon, T. (2018). Oklahoma's induced seismicity strongly linked to wastewater injection depth. *Science*, *359*(6381), 1251–1255. https://doi.org/10.1126/science.aap7911

Jones, C. (2020, January 6). Oklahoma is shaking a lot less from even only a year ago, but still not near historic seismic average. *Tulsa World*. https://www.tulsaworld.com/news/state-and-regional/oklahoma-is-shaking-a-lot-less-from-even-only-a/article_ffb7442c-d9d0-5e1c-a451-6c1647c9fa02.html

Kao, H., Eaton, D. W., Atkinson, G. M., Maxwell, S., & Mahani, A. B. (2016). Technical meeting on the traffic light protocols (TLP) for induced seismicity: Summary and recommendations. *Geological Survey of Canada, Open File*, *8075*, 20.

Keranen, K. M., Savage, H. M., Abers, G. A., & Cochran, E. S. (2013). Potentially induced earthquakes in Oklahoma, USA: Links between wastewater injection and the 2011 Mw 5.7 earthquake sequence. *Geology*, *41*(6), 699–702.

Keranen, K. M., & Weingarten, M. (2018). Induced Seismicity. *Annual Review of Earth and Planetary Sciences*, *46*(1), 149–174. https://doi.org/10.1146/annurev-earth-082517-010054

Keranen, K. M., Weingarten, M., Abers, G. A., Bekins, B. A., & Ge, S. (2014). Sharp increase in central Oklahoma seismicity since 2008 induced by massive wastewater injection. *Science*, *345*(6195), 448. https://doi.org/10.1126/science.1255802

Langenbruch, C., Weingarten, M., & Zoback, M. D. (2018). Physics-based forecasting of man-made earthquake hazards in Oklahoma and Kansas. *Nature Communications*, *9*(1), 3946. https://doi.org/10.1038/s41467-018-06167-4

Langenbruch, C., & Zoback, M. D. (2016). How will induced seismicity in Oklahoma respond to

decreased saltwater injection rates? *Science Advances*, *2*(11), e1601542.

https://doi.org/10.1126/sciadv.1601542

Lee, K.-K., Ellsworth, W. L., Giardini, D., Townend, J., Ge, S., Shimamoto, T., Yeo, I.-W.,

Kang, T.-S., Rhie, J., Sheen, D.-H., Chang, C., Woo, J.-U., & Langenbruch, C. (2019).

Managing injection-induced seismic risks. *Science*, *364*(6442), 730–732.

https://doi.org/10.1126/science.aax1878

Lists, Maps, and Statistics. (2016). USGS New Earthquake Hazards Program.

https://www.usgs.gov/natural-hazards/earthquake-hazards/lists-maps-and-statistics

Liu, T., Luco, N., & Liel, A. B. (2019). Increases in Life-Safety Risks to Building Occupants

from Induced Earthquakes in the Central United States. *Earthquake Spectra*, *35*(2), 471–

488. https://doi.org/10.1193/041618EQS095M

Logg, A., Mardal, K.-A., Wells, G. N., & others. (2012). *Automated Solution of Differential

Equations by the Finite Element Method*. Springer. https://doi.org/10.1007/978-3-642-

23099-8

Loth, C., & Baker, J. W. (2013). A spatial cross-correlation model of spectral accelerations at

multiple periods. *Earthquake Engineering & Structural Dynamics*, *42*(3), 397–417.

https://doi.org/10.1002/eqe.2212

Majer, E., Nelson, J., Robertson-Tait, A., Savy, J., & Wong, I. (2012). *Protocol for Addressing

Induced Seismicity Associated with Enhanced Geothermal Systems* (DOE/EE--0662,

1219482; p. DOE/EE--0662, 1219482). https://doi.org/10.2172/1219482

McGarr, A. (2014). Maximum magnitude earthquakes induced by fluid injection. *Journal of Geophysical Research: Solid Earth*, *119*(2), 1008–1019. https://doi.org/10.1002/2013JB010597

McGarr, A., Bekins, B., Burkardt, N., Dewey, J., Earle, P., Ellsworth, W., Ge, S., Hickman, S., Holland, A., Majer, E., Rubinstein, J., & Sheehan, A. (2015). Coping with earthquakes induced by fluid injection. *Science*, *347*(6224), 830–831. https://doi.org/10.1126/science.aaa0494

McGarr, A., Simpson, D., & Seeber, L. (2002). Case histories of induced and triggered seismicity. In *International Geophysics* (Vol. 81, pp. 647–661). Elsevier. https://doi.org/10.1016/S0074-6142(02)80243-1

Meier, P. M., Rodríguez, A. A., & Bethmann, F. (2015). *Lessons Learned from Basel: New EGS Projects in Switzerland Using Multistage Stimulation and a Probabilistic Traffic Light System for the Reduction of Seismic Risk*. 8.

Novakovic, M., Atkinson, G. M., & Assatourians, K. (2018). Empirically calibrated ground-motion prediction equation for Oklahoma. *Bulletin of the Seismological Society of America*, *108*(5A), 2444–2461.

Petersen, M. D., Morgan P. Moschetti, Peter M. Powers, Charles S. Mueller, Kathleen M. Haller, Arthur D. Frankel, Yuehua Zeng, Sanaz Rezaeian, Stephen C. Harmsen, Oliver S. Boyd, Ned Field, Rui Chen, Kenneth S. Rukstales, Nico Luco, Russell L. Wheeler, Robert A. Williams, & Anna H. Olsen. (2014). *Documentation for the 2014 Update of the United States National Seismic Hazard Maps* (U.S. Geological Survey Open-File Report 2014–1091). https://dx.doi.org/10.3133/ofr20141091

Petersen, M. D., Mueller, C. S., Moschetti, M. P., Hoover, S. M., Llenos, A. L., Ellsworth, W. L., Michael, A. J., Rubinstein, J. L., McGarr, A. F., & Rukstales, K. S. (2016). *2016 one-year seismic hazard forecast for the Central and Eastern United States from induced and natural earthquakes* (USGS Numbered Series No. 2016–1035; Open-File Report). U.S. Geological Survey. http://pubs.er.usgs.gov/publication/ofr20161035

Petersen, M. D., Mueller, C. S., Moschetti, M. P., Hoover, S. M., Rukstales, K. S., McNamara, D. E., Williams, R. A., Shumway, A. M., Powers, P. M., Earle, P. S., Llenos, A. L., Michael, A. J., Rubinstein, J. L., Norbeck, J. H., & Cochran, E. S. (2018). 2018 One-Year Seismic Hazard Forecast for the Central and Eastern United States from Induced and Natural Earthquakes. *Seismological Research Letters*, *89*(3), 1049–1061. https://doi.org/10.1785/0220180005

Petersen, M. D., Mueller, C. S., Moschetti, M. P., Hoover, S. M., Shumway, A. M., McNamara, D. E., Williams, R. A., Llenos, A. L., Ellsworth, W. L., Michael, A. J., Rubinstein, J. L., McGarr, A. F., & Rukstales, K. S. (2017). 2017 One-Year Seismic-Hazard Forecast for the Central and Eastern United States from Induced and Natural Earthquakes. *Seismological Research Letters*, *88*(3), 772–783. https://doi.org/10.1785/0220170005

Petersen, M. D., Shumway, A. M., Powers, P. M., Mueller, C. S., Moschetti, M. P., Frankel, A. D., Rezaeian, S., McNamara, D. E., Luco, N., Boyd, O. S., Rukstales, K. S., Jaiswal, K. S., Thompson, E. M., Hoover, S. M., Clayton, B. S., Field, E. H., & Zeng, Y. (2019). The 2018 update of the US National Seismic Hazard Model: Overview of model and implications. *Earthquake Spectra*, 8755293019878199. https://doi.org/10.1177/8755293019878199

QuickFacts: Texas; Kansas; Oklahoma. (2018). United States Census Bureau.

    https://www.census.gov/quickfacts/fact/table/TX,KS,OK/PST045219

Raleigh, C. B., Healy, J. H., & Bredehoeft, J. D. (1976). An experiment in earthquake control at

    Rangely, Colorado. *Science*, *191*(4233), 1230–1237.

Roach, T. (2018). Oklahoma earthquakes and the price of oil. *Energy Policy*, *121*, 365–373.

Rubinstein, J. L., & Mahani, A. B. (2015). Myths and Facts on Wastewater Injection, Hydraulic

    Fracturing, Enhanced Oil Recovery, and Induced Seismicity. *Seismological Research*

    Letters, *86*(4), 1060–1067. https://doi.org/10.1785/0220150067

Shapiro, S. A. (2015). *Fluid-Induced Seismicity*. Cambridge University Press.

    https://doi.org/10.1017/CBO9781139051132

Skinner, M. (2016a). *Media Advisory—Regional Earthquake Response Plan for Western*

    Oklahoma. Oklahoma Corporation Commission.

    http://www.occeweb.com/News/2016/03-07-16ADVISORY-

    AOI,%20VOLUME%20REDUCTION.pdf

Skinner, M. (2016b). *Media Advisory—Regional Earthquake Response Plan for Central*

    Oklahoma and Expansion of the Area of Interest. Oklahoma Corporation Commission.

    http://www.occeweb.com/News/2016/03-07-16ADVISORY-

    AOI,%20VOLUME%20REDUCTION.pdf

Skoumal, R. J., Ries, R., Brudzinski, M. R., Barbour, A. J., & Currie, B. S. (2018). Earthquakes

    Induced by Hydraulic Fracturing Are Pervasive in Oklahoma. *Journal of Geophysical*

    Research: Solid Earth, *123*(12), 10,918-10,935. https://doi.org/10.1029/2018JB016790

State Area Measurements and Internal Point Coordinates. (2018, August 9). Census.Gov.

    https://www.census.gov/geographies/reference-files/2010/geo/state-area.html

Taylor, J., Çelebi, M., Greer, A., Jampole, E., Masroor, A., Melton, S., Norton, D., Paul, N., Wilson, E., & Xiao, Y. (2017). M5. 0 Cushing, Oklahoma, USA Earthquake on November 7, 2016. In *EERI Earthquake Reconnaissance Team Report*.

Toppozada, T. R., Branum, D. M., Reichle, M. S., & Hallstrom, C. L. (2002). San Andreas Fault Zone, California: M ≥5.5 Earthquake History. *Bulletin of the Seismological Society of America*, *92*(7), 2555–2601. https://doi.org/10.1785/0120000614

U.S. Geological Survey. (n.d.). *Earthquake Catalog*. earthquake.usgs.gov/earthquakes/search

van der Elst, N., Page, M., Weiser, D., Goebel, T., & Hosseini, S. (2016). Induced earthquake magnitudes are as large as (statistically) expected: Induced earthquake maximum magnitudes. *Journal of Geophysical Research: Solid Earth*, *121*. https://doi.org/10.1002/2016JB012818

van Elk, J., Bourne, S. J., Oates, S. J., Bommer, J. J., Pinho, R., & Crowley, H. (2019). A Probabilistic Model to Evaluate Options for Mitigating Induced Seismic Risk. *Earthquake Spectra*, *35*(2), 537–564. https://doi.org/10.1193/050918EQS118M

van Thienen-Visser, K., & Breunese, J. N. (2015). Induced seismicity of the Groningen gas field: History and recent developments. *The Leading Edge*, *34*(6), 664–671. https://doi.org/10.1190/tle34060664.1

Vlek, C. (2019). Rise and reduction of induced earthquakes in the Groningen gas field, 1991–2018: Statistical trends, social impacts, and policy change. *Environmental Earth Sciences*, *78*(3), 59. https://doi.org/10.1007/s12665-019-8051-4

Walters, R. J., Zoback, M. D., Baker, J. W., & Beroza, G. C. (2015). Characterizing and Responding to Seismic Risk Associated with Earthquakes Potentially Triggered by Fluid

Disposal and Hydraulic Fracturing. *Seismological Research Letters*, *86*(4), 1110–1118. https://doi.org/10.1785/0220150048

White, I. J., Liu, T., Luco, N., & Liel, A. B. (2018). Considerations in comparing the US Geological Survey one-year induced-seismicity hazard models with "Did You Feel It?" and instrumental data. *Seismological Research Letters*, *89*(1), 127–137.

Working Group on California Earthquake Probabilities. (1995). Seismic hazards in Southern California: Probable earthquakes, 1994 to 2024. *Bulletin of the Seismological Society of America*, *85*(2), 379–439.

Yeck, W. L., Hayes, G. P., McNamara, D. E., Rubinstein, J. L., Barnhart, W. D., Earle, P. S., & Benz, H. M. (2017). Oklahoma experiences largest earthquake during ongoing regional wastewater injection hazard mitigation efforts. *Geophysical Research Letters*, *44*(2), 711–717. https://doi.org/10.1002/2016GL071685

Yong, A., Thompson, E. M., Wald, D. J., Knudsen, K. L., Odum, J. K., Stephenson, W. J., & Haefner, S. (2016). *Compilation of VS30 Data for the United States* (Report No. 978; Data Series). USGS Publications Warehouse. https://doi.org/10.3133/ds978

Zalachoris, G., & Rathje, E. M. (2019). Ground Motion Model for Small-to-Moderate Earthquakes in Texas, Oklahoma, and Kansas. *Earthquake Spectra*, *35*(1), 1–20. https://doi.org/10.1193/022618EQS047M

Appendix

Table A-1 Area with probability of SFD loss, assuming one repair, exceeding 1% of building value

Scenario	Area (km²) with probability of loss in any motion exceeding 1% of building value	
	P(Exceed) > 10%	P(Exceed) > 50%
Control	406	0
S1	419	0
S2	406	0
S3	395	0
R1	394	0
R2	388	0
R3	388	0
R4	394	0
R5	398	0
R6	383	0

Table A-2 Area with probability of SFD loss, assuming repair after each event, exceeding 1% of building value

Scenario	Area (km²) with probability of total loss exceeding 1% of building value	
	P(Exceed) > 10%	P(Exceed) > 50%
Control	14395	188
S1	14120	84
S2	14211	116
S3	12688	28
R1	14164	147
R2	13206	115
R3	11701	96
R4	14314	156
R5	14124	141
R6	13703	121

Table A-3 Loss to archetypal region

Scenario	Loss	
	Loss from most damaging event	Total loss over two-year simulation
Control	$8,330,000	$15,700,000
S1	$6,290,000	$11,600,000
S2	$6,120,000	$11,700,000
S3	$5,460,000	$9,190,000
R1	$5,300,000	$11,400,000
R2	$5,060,000	$11,300,000
R3	$5,010,000	$9,780,000
R4	$6,550,000	$12,100,000
R5	$6,810,000	$11,500,000
R6	$5,690,000	$11,700,000